Computer-generated holograms for 3D imaging: A survey

ERDEM SAHIN, Tampere University, Finland
ELENA STOYKOVA, Institute of Optical Materials and Technologies, Bulgaria
JANI MÄKINEN, Tampere University, Finland
ATANAS GOTCHEV, Tampere University, Finland

Holography is usually considered as the ultimate way to visually reproduce a three-dimensional scene. Computer-generated holography constitutes an important branch of holography, which enables visualization of artificially-generated scenes as well as real three-dimensional scenes recorded under white light illumination. In this article, we present a comprehensive survey of methods for synthesis of computer-generated holograms classifying them into two broad categories, namely as wavefront-based methods and ray-based methods. We examine their modern implementations in terms of the quality of reconstruction and computational efficiency. As it is an integral part of computer-generated holography, we devote a special section to speckle suppression, which is also discussed under two categories following the classification of underlying computer-generated hologram methods.

CCS Concepts: • **General and reference** → **Surveys and overviews**; • **Human-centered computing** → **Visualization**; • **Hardware** → **Displays and imagers**.

Additional Key Words and Phrases: Computer-generated holograms, 3D displays, 3D imaging

1 INTRODUCTION

The holograms carry intensity, color, depth and directional information of a given three-dimensional (3D) scene and they are able to reconstruct the corresponding true light wavefronts. They provide continuous motion parallax and deliver correct visual cues of binocular disparity, vergence, accommodation (focus) and retinal blur, which are all critical for accurate depth perception. Thus, holographic 3D imaging enables highly realistic visualization and this makes it a very appealing research area.

Advances in digital sensor and display devices as well as computing have introduced new areas into traditional optical (analog) holographic imaging. Significant efforts have been dedicated to development of dynamic holographic displays [Yamaguchi 2016; Yaraş et al. 2010]. Device based limitations still exhibit an important challenge to overcome especially for glasses-free type of visualization due to need for high space-bandwidth product, i.e., correspondingly, wide field of

---

Authors' addresses: Erdem Sahin, Tampere University, Faculty of Information Technology and Communication Sciences, Korkeakoulunkatu 1, Tampere, 33720, Finland, erdem.sahin@tuni.fi; Elena Stoykova, Institute of Optical Materials and Technologies, Bulgarian Academy of Sciences, Acad. Georgi Bonchev Str., Bl.109, Sofia, 1113, Bulgaria, elena.stoykova@gmail.com; Jani Mäkinen, Tampere University, Faculty of Information Technology and Communication Sciences, Korkeakoulunkatu 1, Tampere, 33720, Finland, jani.makinen@tuni.fi; Atanas Gotchev, Tampere University, Faculty of Information Technology and Communication Sciences, Korkeakoulunkatu 1, Tampere, 33720, Finland, atanas.gotchev@tuni.fi.

---

view and wide viewing angle. However, this constraint can be significantly relieved in the case of near-eye or head-mounted display scenarios, intended for virtual or augmented type of visualization. This, already makes holographic imaging a viable option for such displays [Maimone et al. 2017]. Furthermore, compared to other advanced 3D display technologies such as ray-based light field displays including super multiview displays [Takaki and Nago 2010], integral imaging [Xiao et al. 2013] and tensor displays [Wetzstein et al. 2012], holographic imaging and displays have the very crucial advantage that it can accurately reproduce deep 3D scenes.

The scene capture or recording methods for holographic displays can be classified into two broad categories, namely digital holography and computer-generated holography [Tsang and Poon 2016]. Digital holography utilizes optically recorded digital holograms. The need for precise and optically stable coherent illumination setup imposes a strong constraint in such holograms, which usually limits the capability of such holograms to static and small-scale scenes. The second method is based on computational synthesis of so-called computer-generated holograms (CGHs). Computer-generated holography seems to have much greater potential due to the capability of hologram synthesis for synthetically generated computer graphics (CG) objects and real scenes recorded under natural white light.

Besides displaying CGHs on dynamic holographic displays, it is also possible to "print" them onto a physical carrier using lithography. The methods such as HS printing [Brotherton-Ratcliffe et al. 2011] or wavefront printing [Kang et al. 2016b] combine computational and analog holography by recording white-light viewable holograms from digital contents. Combined implementation of both concepts is reported in [Matsushima and Sonobe 2018], where a wave field captured for a real 3D object by means of digital holography is incorporated in a CGH. Application areas of CGHs are not limited to holographic displays. They are also utilized in holographic projection [Buckley 2011], or they can serve as diffractive optical elements for various other purposes such as lens, diffraction grating, combiner, phase spatial filter, beam shaper, optical tweezer (photonic manipulation of particles), etc., which make them useful in various advanced scientific and technological fields as well as industry sectors [Cirino et al. 2011].

In the last two decades, much effort in computer-generated holography has been put on i) improvement of object data encoding in the hologram by more accurate rendering techniques for high-quality reconstructions and ii) fast computation by developing more efficient algorithms and utilizing high-performance hardware. This paper presents a survey of the state-of-the-art in synthesis of CGHs with a focus in this time duration where notable advances have been achieved in the field. The structure of the survey is as follows: Section 2 introduces preliminary theoretical background as well as a short historical overview of CGH synthesis. The theoretical background is supplemented in Appendix A with numerical wave propagation algorithms. We divide the existing CGH methods into wavefront-based and ray-based methods, which are presented in Section 3 and Section 4, respectively, with their pros and cons from the point of view of imaging quality and computational efficiency. These two groups consist of several subgroups, which differ by the type of model employed for 3D scene representation as well as wave propagation method adopted for computing the hologram due to given model. Section 5 discusses the speckle suppression techniques for both wavefront and ray-based CGH methods. Comparative summary of the described methods concludes the paper. Please note that in Appendix B we also provide a supplementary discussion on synthesis and numerical reconstruction of different types of CGHs via simulating the process of CGH viewing by the human eye.

2 BACKGROUND

Holography is a two-step process of recording and reconstruction of the wavefront due to a 3D object under coherent illumination. This wavefront, the so-called object field, is described by a

complex amplitude $O(x, y) = a_0(x, y) \exp[j\phi_0(x, y)]$ on the hologram plane (x, y) at $z = 0$, where $a_0(x, y)$ and $\phi_0(x, y)$ are the amplitude and the phase of the object field, respectively, and j is the imaginary unit. The amplitude gives the intensity of light, while the phase encodes the depth information. The hologram records interference of the object wave with a mutually coherent reference wave, $R(x, y) = a_R(x, y) \exp[j\phi_R(x, y)]$ with amplitude $a_R(x, y)$ and phase $\phi_R(x, y)$ (see Figure 1(a)), as a two-dimensional (2D) distribution of intensity:

$$I_H(x, y) = |R(x, y) + O(x, y)|^2 = RR^* + OO^* + OR^* + O^*R, \tag{1}$$

where the asterisk denotes a complex conjugate operator. The relevant information is encoded in the last two terms, which are referred to as +1 and -1 diffraction orders, respectively. The sum of the intensities of the reference and the object waves, $RR^* + OO^*$, forms the zero-order term, which is usually much brighter than the first-order terms. In a CGH, this zero-order can be discarded and only the relevant object information can be encoded in the hologram resulting in the so-called bipolar intensity distribution [Lucente 1994] as

$$\tilde{I}_H(x, y) = 2\text{Re}\{O(x, y)R^*(x, y)\}. \tag{2}$$

The object wavefront or its conjugate is reconstructed by multiplication of $I_H(x, y)$ with the replica of $R(x, y)$ or its conjugate. That is, for a unit-amplitude reference wave, $OR^*R = O$ or $O^*RR^* = O^*$. This brings into focus the virtual (orthoscopic) image or the real (pseudoscopic) image of the object. Both reconstructed object wavefronts carry the same information content, so they create twin images. In in-line geometry, when $R(x, y)$ and $O(x, y)$ propagate along the same direction, the twin images overlap focusing on the opposite sides of the in-line hologram. This means that in the plane of the focused reconstruction of a virtual image there is a defocused real image and vice versa. Mathematically, the existence of twin images is due to non-linear encoding of complex information as a 2D array of real numbers.
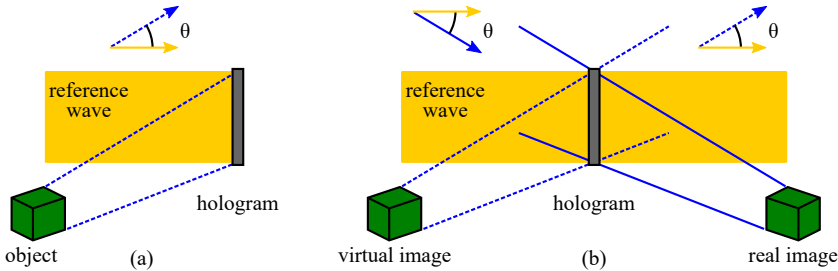

Fig. 1. Holographic recording (a) and holographic reconstruction (b) in off-axis geometry.

The formulation of the holographic principle given by Equation (1) was actually first established with in-line geometry by Dennis Gabor, in 1948. He considered inline illumination of a semi-transparent object with a point light source [Gabor 1948]. Separation of the light beams of the twin images in space was demonstrated later, in 1962, by Leith and Upatnieks [Leith and Upatnieks 1962] via an off-axis geometry, where a spatial carrier frequency was introduced in the hologram through angular separation of the object and reference beams (see Figure 1). Introduction of the carrier frequency shifts the object spectrum from the zero frequency in the spatial frequency domain. This solution decreases the useful space-bandwidth product of the hologram, which is defined as the product of the hologram size and its spatial frequency bandwidth [Claus et al. 2011; Lohmann et al. 1996]. The space-bandwidth product in digital holography characterizes the field of view the

hologram can support. At off-axis geometry, only one-fourth of the space-bandwidth product is practically used.

Synthesis of CGHs basically requires acquiring the 3D information of the scene, i.e., the object field $O(x, y)$. Having found the object field, the CGH itself can be calculated by applying Equation (1) following the in-line or off-axis recording geometry. Thus, the CGH synthesis includes three steps: i) digital representation of the 3D scene; ii) digital propagation of the wave field, i.e., object field, from the scene to the hologram plane; iii) digital encoding of the fringe pattern on the hologram plane in accordance with Equation (1). Over the years, implementation of these steps has created different groups of algorithms.

CGH-based holographic 3D imaging is not a trivial task. Crucial factors for the CGH synthesis are image quality and computational burden. High image quality means ability for high spatial resolution, full color and full parallax photorealistic representation and reconstruction in a wide viewing angle of 3D scenes with shading, reflections and occlusions as schematically depicted in Figure 2. Reconstruction of color, shading and reflection depends on illumination direction, surface properties and orientation. Reflection from an opaque surface is given by bidirectional reflectance distribution function which in general may have components describing ambient, diffuse and specular reflection. Occlusion can be mutual occlusion when an object in a 3D scene blocks the light coming from other object or a self-occlusion when some parts of an object shields its other parts. Such properties constitute view-dependent characteristics of CGHs, and, in addition to provided spatial resolution, they are also crucial to ensure high quality realistic reconstructions. In order to support all those, the CGH must possess a very small pixel pitch and extremely large number of pixels. This entails processing of huge amount of data, which makes computational efficiency of vital importance for CGH synthesis, especially for dynamic imaging.
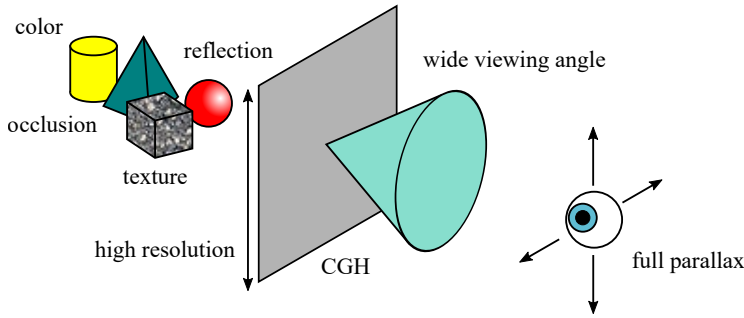

Fig. 2. Requirements for high-quality CGH reconstruction.

Historically, at the beginning of the CGH era, the encoding step dominated the CGH synthesis due to the need of physically fabricating them as optical elements with the required diffractive properties to create the desired visual effect. Design of a CGH as a diffractive optical element followed the development of technology. It started with holograms reproduced by computer plotters as hard copies, which were transferred onto a photographic film in the 1960s, went through photolithographic fabrication in the 1970s and ended with using e-beams in the 1980s. Lohmann's group made the first substantial progress in CGH production technology. Lohmann formulated the idea of encoding a numerically generated hologram in 1956, and various encoding methods such as the "single-sideband" technique and the "detour phase" method [Brown and Lohmann 1966; Lohmann and Paris 1967] emerged in the 1960s to make use of existing computers at that time. In view of inability of the computer plotters for gray-scale drawing, the developed methods

produced binary holograms. The complex amplitude $a_0 \exp(j\phi_0)$ was encoded as an aperture with an area proportional to transmission a_0 where desired phase shift ϕ_0 was achieved through displacement with respect to a regular grating grid. Spatial encoding of complex amplitudes formed the sub-class of cell-oriented holograms [Dallas 1980]. Later, to overcome the limitations of binary holograms, development of different gray-scale or phase-only coding schemes proved that the generated amplitude or phase holograms are capable of reconstructing 3D objects. The amplitude hologram inevitably reconstructs the zero-order and the twin images, whereas the phase hologram reconstructs only the object beam. Encoding of only the amplitude or phase information as 2D arrays of real numbers has allowed for production of point-oriented holograms [Dallas 1980]. These types of holograms are especially suitable for the modern pixelated SLMs.

Nowadays, holographic imaging highly benefits from the fast computer controllable SLMs with large throughput and high diffraction efficiency. Liquid crystal based and mirror based devices constitute the two widely used categories of SLMs [Yaraş et al. 2010]. In the former case, the amplitude and phase of the light are modulated based on the polarization and refractive index characteristics of the crystal, respectively. In the latter case, electro-mechanical control of a micro-mirror array produces the desired amplitude or phase modulation. Besides such devices, in an effort of producing horizontal parallax only real-time holographic display, acousto-optic modulators have been also utilized to achieve light modulation through interaction between acoustic waves and coherent light [St-Hilaire et al. 1990]. Despite the recent developments, there are still two critical issues related with SLMs. The first issue is that the conventional pixelated SLMs can modulate only the amplitude or the phase of the incident coherent light. Full complex modulation has been demonstrated via arrangements including multiple amplitude and phase SLMs [Tudela et al. 2002; Zhu and Wang 2014] as well as a single SLM with additional optical filters [Liu et al. 2011; van Putten et al. 2008]. Actually, long before using SLMs, a referenceless hologram was realized by encoding amplitude and phase information of the complex amplitude in the different layers of a color photographic film [Chu et al. 1973]. On the other hand, on the computational side, the Gerchberg-Saxton algorithm has been widely utilized as an effective method to obtain phase-only holograms, where the phase information is optimized through execution of iterative backward and forward Fourier or Fresnel transform with constraints applied in the CGH and image planes [Gerchberg and Saxton 1972; Stoykova et al. 2013]. To improve the computational efficiency and enable real-time operation, recently several non-iterative approaches have been also proposed that directly compute phase-only holograms based on, e.g., random phase noise averaging [Buckley 2011], sampled phase-only hologram [Tsang et al. 2016], and patterned phase-only hologram [Tsang et al. 2017]. The second issue related with SLMs is that CGH encoding using modern SLMs suffers from the bandwidth limitations imposed by pitch and number of the pixels employed in such devices. These two critical parameters are still far from the values required to provide wide field of view and wide viewing angle visualization. The reconstructed objects from the CGHs fed to SLMs are usually small and must be located at a large distance from the SLM due to the small diffraction angle, which is limited by the pixel pitch of the SLM, Δ, as $\theta_d = 2 \sin^{-1}[\lambda/(2\Delta)]$. In the case of static imaging, better quality can be achieved thanks to the small pixel pitches provided, e.g., via lithography [Igarashi et al. 2018; Matsushima and Nakahara 2009] or by holographic printing on a silver halide plate [Brotherton-Ratcliffe et al. 2011; Kang et al. 2016b].

Long history of CGH synthesis with contributions from many research groups have resulted in partially inconsistent terminology. Being aware of this fact, we divide the existing CGH design methods in 3D imaging into wavefront-based and ray-based methods. The wavefront-based CGH methods calculate the 3D wave field due to a given object or scene, particularly its 2D distribution on the hologram plane, by simulating the diffraction process. The group of the wavefront-based methods mainly relies on scalar wave diffraction and comprises three main categories, which utilize

point cloud, polygon and layered representations of the 3D scene. All such methods utilize 3D positional information of the scene. It is either explicitly available, e.g., in the form of a point cloud, or obtained by some sort of ray tracing for synthetic objects, or extracted from depth estimation in the case of real objects. On the other hand, the ray-based CGH methods form the hologram from incoherently captured 2D images of the 3D scene. That is, they rely on geometric (ray) optics formalism of light and conversion from ray-based representations to wavefront-based holographic information. The ray-based methods comprise two important categories, which are the holographic stereogram (HS) and multiple viewpoint projection (MVP) holography. Depending on the capture setup and encoding scheme, the acquired ray intensities are utilized to generate either a coherent CGH that includes coherent object field information (e.g., MVP), or its incoherent approximation (e.g., HS). The following sections discuss wavefront-based and ray-based CGH methods in detail. Please, refer to Appendix A for a theoretical background on numerical wave propagation algorithms, which are widely utilized in CGH synthesis.

3   WAVEFRONT-BASED CGH METHODS

The wavefront-based methods simulate optical wave propagation to calculate the 3D wave field due to a given 3D scene or object illuminated by a coherent light source. With further implementation of the interference process between the object field and a reference wave, the optical holographic recording process given in Equation (1) is fully simulated. The preparation of the geometrical 3D object information is the very first critical step of CGH generation. The object can be a collection of independent light sources as points or planar segments, or sliced into layers. The dense depth sampling of the scene can be made e.g., via ray casting or ray tracing.

Both the form of the utilized geometric object information and the accuracy of the adopted diffraction model are important factors determining the qualitative characteristics (such as reconstructed image quality, smoothness of parallax, handling of occlusions, etc.) of a given wavefront-based method. Besides accuracy, the computational complexity of the CGH generation is another key factor that has been extensively addressed in the CGH literature. We categorize the wavefront-based methods and discuss the distinctions between various methods under each category based on these factors. In particular, we divide the wavefront-based methods into three main categories: i) Point cloud model, ii) Polygon-based model, iii) Layer-based model.

3.1   Point cloud model

General implementation. One of the most widely used object representations is the point cloud model proposed for the first time by Waters in 1966 [Waters 1966]. According to this model, the 3D object can be represented as a collection of self-emitting point sources of light, which act independently. The wave emitted from the object is formulated as superposition of spherical waves corresponding to such point sources, i.e., the complex amplitude on the hologram plane is found as

$$O(x, y) = \sum_{p=1}^{P} \frac{A_p}{r_p} \exp(jkr_p), \tag{3}$$

where $A_p = a_p \exp(j\phi_p)$ gives the wave field emanated by point source p having real-valued amplitude a_p and phase ϕ_p, $r_p = \sqrt{(x - x_p)^2 + (y - y_p)^2 + z_p^2}$ is the distance between this point source at (x_p, y_p, z_p) and the point $(x, y, 0)$ on the hologram plane located at $z = 0$, P is the total number of point sources and $k = 2\pi/\lambda$ is the wavenumber. It is worth to note that the propagation model given by Equation (3) corresponds to the Rayleigh-Sommerfeld diffraction model without the obliquity factor (see Equation (A.3) in Appendix A). Considering a unit amplitude plane wave $R(x, y)$ normally incident on the hologram plane, the interference pattern due to the object field

given by Equation (3) can be written in the form of bipolar intensity distribution as

$$\hat{I}_H(x, y) = \sum_{p=1}^{P} \frac{a_p}{r_p} \cos\left(\frac{2\pi}{\lambda} r_p + \phi_p\right) = \sum_{p=1}^{P} a_p T(x, y, x_p, y_p, z_p). \tag{4}$$

The point cloud model is the most flexible method for 3D object representation. In the reconstruction, it creates highly realistic full-parallax color images of 3D objects with arbitrary shapes at high spatial and angular resolutions. The density of the point sources should satisfy the acuity requirement of the human visual system (HVS). That is, the lateral distance between the neighboring object points subtends an angle of no more than 1/60 degrees at the viewer's eye positioned at the intended viewing depth [Born 1999]. This ensures smooth (continuous) perception of surfaces. The point cloud model is suitable for virtual and real objects; in the latter case, the point cloud is an output of profilometric or tomographic capture [Stoykova et al. 2013]. It also serves well for generation of specific types of holograms, such as image-plane hologram [Yamaguchi and Yoshikawa 2011] and cylindrical hologram [Yamaguchi et al. 2007]. Furthermore, it allows for parallel processing and utilization of field programmable gate arrays (FPGAs) and graphics processing units (GPUs) as well as clusters of these devices [Jackin et al. 2018]. The memory allocated for implementation of the point cloud method contains only the 3D scene data and the output hologram.
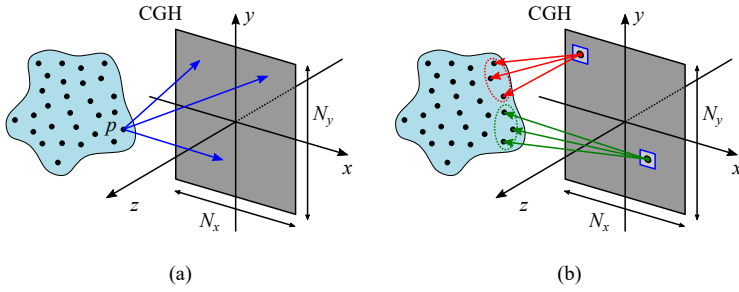

Fig. 3. Point cloud model for CGH generation: (a) object-oriented approach with ray-tracing from a fixed set of object points to the CGH samples; (b) image-oriented approach with ray-casting from the CGH samples and forming different sets of point sources for different parts of the CGH.

Many authors refer to the point cloud method as a ray-oriented, ray-tracing or coherent ray-tracing method [Ichikawa et al. 2013a; Waters 1966; Wei et al. 2016], since all possible rays between a point source and a hologram sample are traced in the hologram calculation. The CGH in the point cloud method consists of overlapping Fresnel zone plates, i.e., $T(x, y, x_p, y_p, z_p)$, $p = 1, 2, \ldots, P$. In the basic implementation, the *object-oriented* or *object order approach* propagates the complex amplitudes from a fixed set of point sources representing the 3D scene to the points on the hologram plane (see Figure 3(a)). This straightforward implementation has difficulties in modeling the view-dependent image quality factors such as occlusion and parallax, and view-dependent shading. For instance, in an approximate occlusion culling method implemented in [Chen and Wilkinson 2009], the visibility of each point source from each hologram sampling location is determined based on an approximate visibility formula. Those points that are found to be occluded are then discarded in the CGH calculation. On the other hand, in the *image-oriented* or *image order approach*, illustrated in Figure 3(b), the CG techniques such as ray casting and ray tracing are employed to better handle all such view-dependent factors. In [Zhang et al. 2011], the CG ray-casting technique is used for hidden surface removal. The rays are cast from each sample of the hologram within the diffraction angle determined by the hologram sampling. For each hologram sample, a set of visible points

are determined. Such an approach is very effective for expressing the occlusion effect. The ray casting approach introduced in [Ichikawa et al. 2013a] utilizes a coarser viewpoint sampling on the hologram plane. The hologram is divided into a set of elemental hologram segments and the center of each segment is chosen to be a viewpoint to cast rays within the diffraction angle of the hologram. The angular resolution of rays cast from each viewpoint is set to satisfy the requirement of visual acuity. The developed approach is able to express a combination of image properties such as shading, shadowing, multi-reflection and refraction. There are several other methods, e.g., proposed before in [Smithwick et al. 2010] and later in [Zhang et al. 2015], that are very similar to the ray casting introduced in [Ichikawa et al. 2013a]. The common feature of all such methods is that the view-dependent intensity of the scene is sampled on a regular grid on the hologram plane together with depth information for each back projected ray. The coherent wave contribution of each point to each segment is then calculated based on the knowledge of positional and amplitude information. In [Ichikawa et al. 2013b], such an approach builds a CGH for a Fourier transform optical system to enlarge the field of view. Especially for scenes including multiple 3D objects, a multi-plane occlusion processing by means of multiple point cloud sampling planes is proposed in [Jia et al. 2014]. The occlusion culling is achieved based on the orthographic projections along differently oriented sampling planes. After hidden surface removal, the projected images are back-projected to the object domain and then conventional point cloud model is used for CGH synthesis.

The image-oriented approach is actually a sampling process, where the positional and/or view-dependent intensity information of a 3D object is sampled from different viewpoints as traced on the hologram plane. It is most likely that for each viewpoint, a different set of object points are sampled. As a consequence of that, the coherent wave contribution of a sampled point source is not fully represented on the entire hologram plane. Thus, although image-oriented approaches provide an efficient way of expressing view-dependent quality factors of the CGHs as discussed above, this sampling issue should be noted as their main drawback, which needs to be further addressed.

Acceleration methods. The high computational complexity of the point cloud model is its main drawback. Implementation of Equation (4) requires $\alpha P N_x N_y$ operations, where α is the number of the executed arithmetic operations for calculation of a cosine, square root, additions and multiplications and $N_x \times N_y$ is the size of the CGH [Shimobaba et al. 2009]. Since the representation of solid shapes needs extremely fine sampling, the computation time can be unacceptable in some cases. Therefore, development of accelerated computation has become an integral part of the implementation of this model. The pros and cons of the recently advanced methods for accelerated point-cloud based computation are thoroughly analyzed in [Tsang et al. 2018].

A straightforward way to accelerate hologram computation is to encode the view-dependent properties only in the horizontal direction resulting in so-called horizontal-parallax-only (HPO) holograms. By this way, an order of magnitude acceleration can be achieved [Lucente 1994; Plesniak et al. 2006]. In [Juárez-Pérez et al. 1997] the four-point symmetry of the Fresnel kernel is utilized to accelerate the computation by a factor of 4. In [Matsushima and Takai 2000] recurrence formulas are derived to accelerate computation of the depth-related phase.

An effective acceleration method is to compute the possible contributions of (unit-amplitude) point sources, i.e., separate terms in Equation (4), off-line and store them in a *look-up-table* (LUT). The composed LUT stores precalculated unit amplitude 2D fringe patterns, $T(x, y, x_p, y_p, z_p)$, $p = 1, 2, \ldots, P$ for all possible object points. In addition, the phases ϕ_p are set to zero for all points [Lucente 1993]. Computation of the CGH requires again $P N_x N_y$ loops but with only one addition and one multiplication for each loop. If the memory attributed to store one pixel of a fringe pattern corresponding to an object point is M_Δ, the memory requirement for the LUT storage is $M_\Delta P N_x N_y$,

which is in the range of terabytes. Therefore, despite accelerated computation, the computational complexity remains to be high.
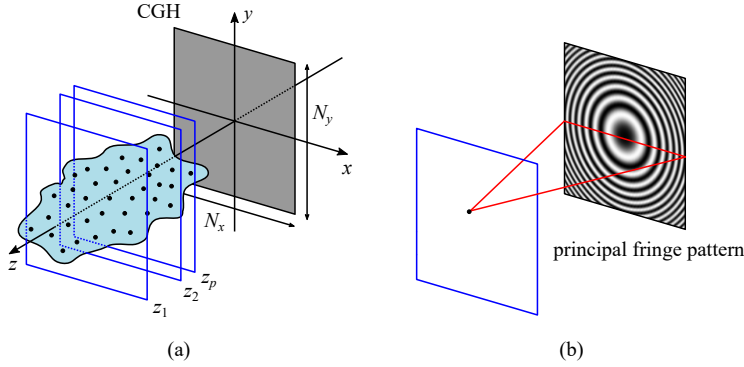

Fig. 4. Schematic representation of the NLUT method (a) and generation of the principal fringe pattern for a given depth (b).

A novel LUT (NLUT) method is proposed in [Kim and Kim 2008] with substantially reduced number of precalculated fringes. The method slices the object by using a set of planes located at different depths along the z-axis (see Figure 4). A plane at a given depth z_p contains a certain number of point light sources, but only the so-called unit amplitude principle 2D fringe pattern, $T(x, y, 0, 0, z_p)$, corresponding to the point source at the center of the plane is precalculated and stored. The fringe patterns of the other light sources on the plane are found by shifting the principle fringe in the hologram plane. The size of the principal fringe pattern is large enough to enable shifts for all possible points. The CGH is obtained by summation of all shifted fringes in all planes, and the memory size is reduced to gigabytes. The NLUT method is based on the shift-invariance of the fringe patterns for points (assigned to be) at the same depth. For holographic video, removing points that do not change in consecutive images and generating CGHs for the residual images is proposed in [Kim et al. 2008b]. Compression efficiency depends on the speed of the objects motion and the method becomes ineffective, if the residual image contains more than 50% of the points in the original images. Higher compression is achieved through evaluation of displacements of objects between two consecutive images along the x-axis and y-axis and then utilization of the estimated motion vectors for motion compensation [Kim et al. 2013]. The drawbacks of this approach are the need for segmentation of the 3D scene for accurate estimation of motion vectors and the decrease of accuracy of this estimation for faster moving objects. Complexity of the task increases for a 3D scene consisting of objects moving at different speeds. For improving the accuracy of motion estimation and compensation, an MPEG-based algorithm is developed in [Dong et al. 2014a] that removes temporal redundancy of the object data. As the data extraction relies not on estimation but on a mathematical model of the 3D scene, the algorithm shows excellent performance when there is more than 50% difference between the points in consecutive images. Because of the shift-invariance property in the lateral direction, the MPEG-based method is not effective for objects with large depth variation. To enable motion compensation in the z-direction, a thin lens property of the Fresnel zone plate is used in [Dong et al. 2014b] to achieve shift-invariance in the z-direction by multiplying two zone plates corresponding to different depths. The result is 3D motion compensation. Compression of the object data for encoding in a set of CGHs by various algorithms is a preprocessing step in NLUT CGH synthesis [Kwon et al. 2016]. For real-time synthesis of a set of CGHs, the composed LUTs need the usage of FPGAs or GPUs [Kwon et al. 2016]. This

requires ensuring software and memory compatibility with the GPU structure, which is achieved by implementing an object tracking mask method. Further improvement of the NLUT method by decomposing the 2D principal fringe patterns into a set of one-dimensional (1D) sub-principal fringe patterns is proposed in [Kim et al. 2012]. Generation of a full-color CGH by using tunable NLUT is developed in [Kim et al. 2015].

The split LUT (SLUT) approach proposed in [Pan et al. 2009] builds separate LUTs for modulation factors along the x-axis and y-axis at a given depth. Under the assumption of a small size of the reconstructed image compared to the distance between the scene and the hologram, the contributions $T(x, y, x_p, y_p, z_p)$ of point sources in Equation (4) can be written as a multiplicatively separable function, i.e., as a product of two terms depending on $(x - x_p)$ and $(y - y_p)$, respectively. This allows decreasing the memory usage and computation time in comparison with the ordinary LUT approach. For a line along the y-axis with n point sources, the number of loops for the CGH synthesis decreases from $nN_x N_y$ to $nN_y + N_x N_y$ [Pan et al. 2009]. The method is further evolved by introducing basic 1D modulation light factors based on the Fraunhofer approximation [Jia et al. 2013] and composing the so-called compressed LUT (CLUT). The SLUT and CLUT are used for accelerated computing of a gigabyte hologram by applying several GPUs controlled by a CPU and CUDA architecture with a dynamic parallelism in [Zhang et al. 2016b]. The authors admit that using a GPU is much more effective for processing floating type data. Although the SLUT method demonstrates substantial acceleration for regularly sampled objects such as planar images, it is not that effective for arbitrarily sampled objects and large size holograms. An improved LUT method for the case of arbitrarily sampled 3D objects is developed in [Wei et al. 2016], where a distance-dependent phase factor, $\exp(jkr_p)$, is introduced and the LUTs of precomputed phase values of successive slices of the 3D object are built. An acceleration method, which takes advantage of the concentric redundancy of the Fresnel zone plate created by a point light source on the CGH plane, is proposed in [Lee et al. 2016; Nishitsuji et al. 2012; Su et al. 2016]. The method calculates the distribution of the complex amplitude along a single radial line of a zone plate corresponding to a given depth, where the length of the line is limited based on the maximum diffraction angle. In [Nishitsuji et al. 2012] this is done by recurrent formulas derived from the relation of adjacent phases. Fast CG technique is developed for drawing a discrete circle in order to roll the calculated line and to form a zone plate. The zone plates are stored in a LUT. The stored plate for a given depth is translated correspondingly to positions of other point sources in the same plane. The developed CG algorithm requires random memory access and is prone to errors. This drawback is removed in [Nishitsuji et al. 2015]. In [Su et al. 2016] CG is also used to roll the complex amplitude distribution along a line around the center of the zone plate, whereas in [Lee et al. 2016] a point source CGH is calculated by linear interpolation. The effects of sampling along the radial line and interpolation on the quality of reconstruction are also studied in [Lee et al. 2016]. Numerical simulations prove efficiency of the approach. Further 10 to 20 times compression of the LUT corresponding to the radial symmetry interpolation method is proposed in [Jiao et al. 2017] by using principal component analysis.

In [Yamaguchi and Yoshikawa 2011], acceleration of computation is achieved via *image-plane holography*, where the location of the 3D object is near the hologram and a given point light source on the object surface contributes to a small spatial window on the CGH plane within the diffraction angle supported by the hologram (see Figure 5(a)). The computational complexity is given by $O(\alpha P(R/\Delta)^2)$, where R is the average radius of such windows [Shimobaba and Ito 2017]. The drawback of this method is that the reconstruction, which corresponds to an image-plane hologram, is located in the vicinity of the hologram plane. It is advanced in [Shimobaba et al. 2009] to reconstruct holograms in the Fresnel region by introducing a *wavefront recording plane* (WRP) close to the 3D objects (see Figure 5(b)). The complex amplitude of the wavefront due
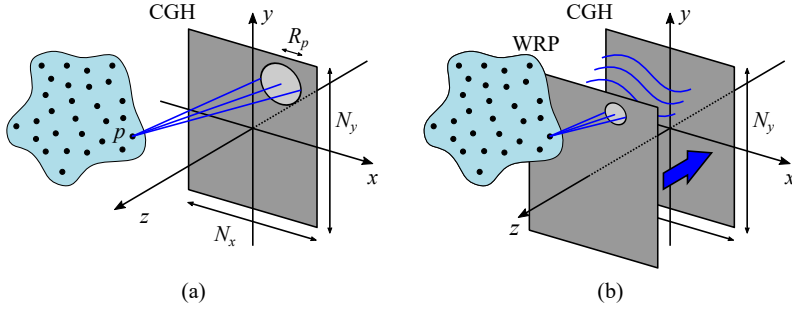
Fig. 5. Computation of an image plane CGH (a) and acceleration of computation by using a wavefront recording plane (b).

to point cloud is calculated at this plane. The wave field due to each point source cover a small area on the WRP (limited by the maximum diffraction angle) and this decreases the number of hologram sampling points taken into consideration. The complex amplitude at the CGH plane is found by Fresnel transform of the complex amplitude on the WRP. For $N_x = N_y$, the computational complexity is evaluated to be $O(\alpha P(R/\Delta)^2) + O(\beta N_x^2 \log N_x)$, where β is the number of arithmetic operations in fast Fourier transform (FFT). For large P the first term dominates. The LUT and WRP methods are combined in [Shimobaba et al. 2010]. The LUT is applied for calculation of the complex amplitude on the WRP plane. Additional acceleration is achieved by using a GPU for propagation from the WRP to the plane of the hologram. Real-time synthesis of a large hologram by GPU implementation of the WRP method is reported in [Weng et al. 2012]. Using multiple WRP planes is proposed in [Phan et al. 2014] for reconstruction of deep scenes. Change of intensity at a single object point affects the whole hologram. Real-time relightening of the reconstructed image without CGH recalculation is proposed in [Tsang et al. 2012] by applying intensity modulation to the WRP. The GPU implementation of this method provides generation of 2K×2K hologram for less than 20 ms. Generation of the WRP directly from a planar intensity image with a Fresnel kernel is proposed in [Tsang and Poon 2015]. The depth related resampling of the WRP encodes the 3D information. The method enables generation of large holograms (2K×2K pixels) of dense objects with rich texture at 100 frames per second. Two WRPs located in front of the objects are used. In [Okada et al. 2014], a discrete set of depths is used with introduction of several WRPs across the point cloud. Backward and forward propagation are utilized. In [Symeonidou et al. 2015], a set of multiple WRPs that slice the point cloud is introduced. This allows choosing the closest WRP for a given point source and to minimize the corresponding spatial support on the WRP for that source. The backward and forward propagation kernels are stored in LUTs for a discrete set of depths. Gaussian interpolation in WRPs blurs the discrete points to simulate propagation of a smooth wavefront surface to the CGH plane. Inverse Gaussian filters mask the occluded points. In [Symeonidou et al. 2018], a Phong illumination model is incorporated in the precomputed LUTs for creation of photorealistic reconstruction. At fixed number of WRPs with predetermined distances between them, the computation time varies depending on the distribution of points in the point cloud. Automatic optimization of the number and locations of WRPs is proposed in [Hasegawa et al. 2017]. A wavelet shrinkage method, which is named as WASABI, is proposed and applied in [Arai et al. 2017; Shimobaba and Ito 2017] to represent the complex amplitudes with a few wavelet coefficients for faster computation [Gilles et al. 2016]. Additional acceleration of computation on GPU with a factor of 30 over conventional approach and improvement of quality of reconstruction compared to WASABI method is reported in [Blinder and Schelkens 2018] by using a sparse basis

representation in the short-time Fourier space. Analysis of the WRP implementation with a single plane or multiple planes is made in [Tsang and Poon 2016].

The so-called *phase-added stereogram* (PAS) approach, first proposed in [Yamaguchi et al. 1993], accelerates the computation of a CGH by sampling the directional information through approximation of the spherical wavefronts of the point sources with a set of planar wavefront patches. The first step in PAS computation is partitioning of the hologram into $M \times N$ equal size square segments, i.e., holographic elements (hogels), with $S \times S$ pixels. The contribution of point p from the point cloud to the segment (m, n), $m = 1, 2, \ldots, M; n = 1, 2, \ldots, N$ with a central point at (x_c^{mn}, y_c^{mn}) is given by the 2D complex sinusoid of $(A_p/r_p) \exp(j\Phi_p^{mn}) \exp[j2\pi(u_p^{mn}x' + v_p^{mn}y')]$, where (x', y') are the local spatial coordinates defined with respect to (x_c^{mn}, y_c^{mn}). The spatial frequencies (u_p^{mn}, v_p^{mn}) of this sinusoid are constant across the segment at a given wavelength and are found with respect to the segment central point. The phase of the sinusoid, $\Phi_p^{mn} = \phi_p + kr_p^{mn}$, is a sum of the phase ϕ_p of the wave due to the point p and a phase related to the distance r_p^{mn} between the point p and the central segment point. The distance related phase is added to match the wavefronts of the plane waves diffracted from all segments. The segment size, $S\Delta \times S\Delta$, where Δ is the pixel size at the hologram plane, should be small enough to well approximate the spherical wavefront emitted by the point p with a plane wave across the segment. The fringe pattern across a segment due to all object points is a superposition of 2D complex sinusoids and can be calculated by a single inverse Fourier transform of the spectrum of the segment built by placing the complex amplitudes of the sinusoids to their locations in the spatial frequency domain. Accelerated computation of the hologram requires applying inverse FFT at the expense of quantization in the frequencies of complex sinusoids. Especially for small size segments, the quantization of frequencies can strongly reduce the reconstruction quality due to resulting inaccurate light steering. Over the years, different improvements of the PAS method have been proposed. The first improvement is the compensated phase-added stereogram (CPAS) algorithm [Kang et al. 2007], which improves the steering by phase compensation introduced to all sinusoids. The compensation contains the difference between the spatial frequencies in the continuous and the discrete domains. The CPAS provides better reconstruction in comparison to that of the PAS with FFT practically without increase of the calculation time. To satisfy the controversial requirements set on the segment size, the accurate PAS (APAS) is developed in [Kang et al. 2008a]. The idea is to calculate the FFT in a larger area than the segment and to increase resolution in the sampled spatial frequency domain. The hologram segment is obtained by truncation. The later accurate compensated PAS (ACPAS) combines both improvements by merging phase compensation and directional error reduction into a single step [Kang et al. 2008b] and produces higher quality reconstructions compared to the previous versions. The fast PAS (FPAS) proposed in [Kang et al. 2016a], applies better phase compensation to ACPAS, where the point p contributes to the segment (m, n) by $(A_p/r_p) \exp\left(j\Phi_p^{mn}\right) \exp\left[j2\pi\left(u_p^{mn}x' + v_p^{mn}y'\right)\right] \exp\left\{j2\pi\left[u_p^{mn}\left(x_c^{mn} - x_p\right) + v_p^{mn}\left(y_c^{mn} - y_p\right)\right]\right\}$. Since the FPAS demonstrates finer beam steering than the other PAS approximations, it provides higher peak intensity and larger peak signal-to-noise ratio in calculating the Fresnel zone plates corresponding to point sources. The recent work overlapp-add stereogram (OLAS) [Padmanaban et al. 2019] uses similar phase compensation to PAS, but unlike in all abovementioned methods, the segments are chosen to be overlapping with single pixel shift. By this way depth-independent high resolution reconstructions are achieved, which is advantageous for deep 3D scenes where the optimal hogel size of conventional PAS methods usually depends on depth. The phase compensated stereogram methods combine well with the ray casting approach, and thus, they allow implementation of visibility tests for handling occlusions.

3.2 Polygon-based model

General description. The other popular model in CGH computation is polygonal representation of 3D objects. Representation of object surface with light sources of planar primitives is the basis for polygon-based models [Leseberg and Frère 1988; Tommasi and Bianco 1993]. In the polygon-based 3D model, the non-planar object is given by a mesh of P light sources with a polygonal shape (e.g., triangle). Each polygon represents an aperture that becomes a source of the object wave field and the wave fields from all polygons are superposed at the plane of the hologram; that is why this method is characterized as a field-oriented approach in [Matsushima and Nakahara 2009].
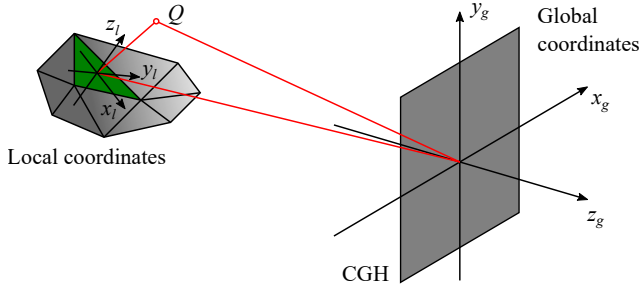

Fig. 6. Schematic representation of the polygon-based CGH computation approach, where the hologram plane is placed at $z_g = 0$ with respect to the global coordinate system and a local coordinate system is utilized on each polygon.

Over the last fifteen years two types of polygon-based CGH algorithms have emerged that are classified as numerical and analytical. In both approaches, a global coordinate system (x_g, y_g, z_g) is introduced with the hologram located in the $(x_g, y_g, z_g = 0)$ plane (see Figure 6). The object field at the hologram plane is found by summing up the wave fields produced by all P polygons:

$$O(x_g, y_g, z_g = 0) = \sum_{p=1}^{P} U^p(x_g, y_g, z_g = 0). \tag{5}$$

In both approaches the polygon fields, $U^p(x_g, y_g, z_g = 0)$, $p = 1, 2, \ldots, P$, are calculated by the angular spectrum method (ASM), see Equation (A.4) in Appendix A, but the angular spectra of the polygons are computed in a different manner. For this purpose, a local coordinate system (x_l, y_l, z_l) is defined on the given polygon with a z_l-axis oriented along its normal and the polygon located at $(x_l, y_l, z_l = 0)$ plane. This system is unique for each polygon. As the polygon plane is tilted with respect to the hologram plane, the formulas describing propagation of a wave field between parallel planes are not directly applicable to the synthesis of a CGH. Rotational transformation is required to relate the plane of a polygon to a plane parallel to the hologram [Matsushima 2008; Matsushima et al. 2003].

Considering an arbitrary point Q as shown Figure 6, the relation between its global and local position vectors $\vec{r}_g$ and $\vec{r}_l$, respectively, can be defined through rotation and translation as [Park 2017]

$$\vec{r}_l = \mathbf{R}\vec{r}_g + \vec{t}; \; \vec{r}_l = \begin{bmatrix} x_l \\ y_l \\ z_l \end{bmatrix}, \; \vec{r}_g = \begin{bmatrix} x_g \\ y_g \\ z_g \end{bmatrix}, \; \vec{t} = \begin{bmatrix} t_x \\ t_y \\ t_z \end{bmatrix}, \; \mathbf{R} = \begin{bmatrix} \vec{n}_{x_l}^T \\ \vec{n}_{y_l}^T \\ \vec{n}_{z_l}^T \end{bmatrix}, \tag{6}$$

where $\mathbf{R}$ is a 3×3 rotation matrix with rows denoting the representation of unit vectors of the local coordinate in the global system and $\vec{t}$ is a translation vector. Please note that the polygon index p is

omitted in the formulas for convenience. The relation between the angular spectra of the wave field on the planes $(x_g, y_g, z_g = 0)$ and $(x_l, y_l, z_l = 0)$, i.e., $G_g(u_g, v_g)$ and $G_l(u_l, v_l)$, respectively, can be obtained as [Park 2017]

$$G_g(u_g, v_g) = \frac{w_l}{w_g} G_l(u_l, v_l) \exp[j2\pi(u_l t_x + v_l t_y + w_l t_z)], \tag{7}$$

where $w_l = \sqrt{(1/\lambda)^2 - u_l^2 - v_l^2}$ and $w_g = \sqrt{(1/\lambda)^2 - u_g^2 - v_g^2}$. The Fourier transforms of the angular spectra of all polygons then give the corresponding object fields $U^p(x_g, y_g, z_g = 0)$, $p = 1, 2, \ldots, P$.

Numerical approach. In the numerical algorithm, a complex function called a property or surface function describes each polygon. The amplitude of this function gives the polygon shape and texture. The phase distribution describes the reflection model, e.g., a random phase can be introduced on each surface function [Matsushima 2005a] to create diffuseness and hence to ensure a wide viewing angle for the polygon. Effective numerical implementation of ASM requires double FFT. The first FFT is executed on a regular sampling grid in the local coordinate system to find the angular spectrum of each surface function. Usage of FFT entails remapping of Fourier coefficients for each polygon when going from the tilted polygon to the global coordinate system. This is due to the rotational transformation, which introduces a shift of the spectrum in the Fourier domain corresponding to the rotated coordinate system and may require interpolation to ensure regular sampling grid in the spatial frequency domain after rotation [Matsushima et al. 2003]. This grid is unique for each polygon, because it is composed according to the geometry of the polygon with respect to the hologram plane. Compensation of the shift in order to place the spectrum into the origin of the rotated system is equivalent to forcing the emitted light to propagate in the direction of z_g-axis. This procedure combined with resampling and bilinear interpolation in the Fourier space is called remapping. Computing the contribution from a single polygon field takes more time than computing a spherical wave from a point source. Nevertheless, the polygonal model offers substantially faster CGH synthesis due to much smaller number of polygons required to represent the object in comparison to the number of point sources in the point cloud model. Therefore, the method is appropriate for synthesis of CGHs of large objects. Remapping is the most computationally extensive step in this FFT-based approach. According to the estimation in [Matsushima 2006], it can take up to 44% of the CPU time. Parallel computation with advanced computing hardware can accelerate the numerical algorithm [Ahrenberg et al. 2006]. Numerical propagation of the wave fields requires storing the complex functions as 2D arrays with the size of the hologram, and hence, restricts the number of pixels in the CGH. Solution to this problem is proposed in [Matsushima and Nakahara 2009] by partitioning the hologram into segments.

Numerical implementation of the polygon-based approach is highly suitable for CGHs providing photorealistic reconstruction. A complex function expressing brightness, surface roughness and illumination conditions characterizes each polygon. Including the object surface properties in the algorithm does not slow down the hologram computation [Lee et al. 2014]. A hidden-surface removal algorithm is demonstrated in [Matsushima 2005b] where a brightness model of the planar surfaces is proposed for introducing desired shading. The idea is based on using a silhouette mask. The method imitates the phenomenon of seeing the light coming from the front surface of the object, $O(x, y)$, and the background field that is not blocked by the object. The latter is found by using a binary mask, $M(x, y)$, which is zero inside the silhouette of the object and unity otherwise. The plane (x, y) coincides with the maximal cross-section of the object for a given viewing direction. Then, for a background wave field, $b(x, y)$, the observed field is $M(x, y)b(x, y) + O(x, y)$. This field is propagated to the hologram plane for the given viewing direction. For multiple objects, the masking procedure is applied to each object and is called object-by-object shielding. It requires

low computational costs and is highly appropriate for processing of mutual occlusions. However, this procedure fails in treating self-occlusions when some parts of an object shield its other parts. To avoid occlusion errors in the case of concave surfaces, the silhouette method is applied to polygons themselves and so is transformed into polygon-by-polygon light shielding. The latter is robust, but is very time-consuming due to the requirement of propagating the wave fields given by $M(x,y)b(x,y) + O(x,y)$ for each polygon, where the surface area of polygons are much smaller than the area occupied by the whole wavefront. Acceleration of calculation for the polygon-by-polygon method is proposed in [Matsushima et al. 2014] by developing a switch-back technique that considers each polygon as a silhouette-shaped aperture.

The polygon-based model facilitates modeling of reflectance distributions by encoding them into the phase of the property function. As in CG, the ratio between the specular and diffuse reflection varies for each object material. Different CG reflection models such as the Phong reflection model, the Cook-Torrance reflection model and others are applied. A method based on Blinn and Torrance-Sparrow reflection models in CG is proposed in [Yamaguchi and Sakamoto 2009] to express reflection distributions, which correspond to arbitrary illuminations, and to include background reflections, which occur when metallic or mirror surfaces are present in the object. This study continues in [Yamaguchi et al. 2011b] by analysis of how the surface roughness affects the reflection distributions. An accurate but time-consuming description of reflectance distributions in CGHs is provided in [Ichikawa et al. 2011] by using a finite difference time-domain method. The Phong reflection model is used in [Nishi et al. 2011] with emphasis on fast computation for synthesizing a high-definition CGH. Because the bandwidth of the spectrum for a specular surface is narrower than the spectrum for a diffusely reflecting surface, the surface function of each polygon is modified in accordance with the Phong model to render specular surfaces. The holograms for reflected images are computed and applied as property functions in [Cho et al. 2015]. Methods for reduction of phase mismatches on the boundaries in the polygonal mesh are also proposed [Im et al. 2015; Liu et al. 2010]. To remove angular appearance of the object surface during reconstruction, a smooth shading is proposed in [Yamaguchi et al. 2011a] by expressing a patch as a curved surface. A CGH of size 8K × 4K is calculated in [Yamamoto et al. 2010] by directly applying CG rendering techniques in case of illumination by a point light source and ambient light.

Analytical approach. Analytical computation of the polygons' spectra can strongly accelerate the polygon-based method. In case of a triangular mesh, the angular spectrum of an arbitrary size and orientation triangle is related to the angular spectrum of a unit-amplitude reference triangle through affine transformation [Ahrenberg et al. 2008; Kim et al. 2008a]. The 3D object is a mesh of triangles and the angular spectra of the wave fields coming from them are computed without performing FFTs in the local coordinate systems. All computations are performed analytically in the continuous domain in the global coordinate system. A uniform sampling grid is used only in the hologram plane, where a single FFT is executed to transform the sum of the angular spectra from the triangular mesh to the object wave field at the hologram plane. No remapping is required in the analytical method, which makes it potentially very fast for CGH synthesis. The fully analytical approach with flat amplitude distributions is derived in [Ahrenberg et al. 2008] by using a right triangle as a reference. A carrier plane wave illuminates each triangle and it reconstructs a wave field with uniform amplitude depending on the illumination direction and the normal vector to its surface. Accuracy of formulas derived in [Ahrenberg et al. 2008] is analyzed and improved in [Pan et al. 2013; Zhang et al. 2013, 2018]. Practically concurrently with Ahrenberg *et.al.*, a semi-analytic model of a wave field emitted by a 3D triangular mesh is introduced in [Kim et al. 2008a]. The angular spectrum of an arbitrary triangle is calculated at the direction of the illumination given by a carrier plane wave through representing the triangle as a sum of two right triangles. Surface

diffuseness is also included in the model by dividing each triangle in the local coordinate system into a set of $m(m-1)/2$ similar small triangles with different amplitudes and phases of the complex wave field, where m is an integer number. The angular spectrum of each triangle is found as a sum of the spectra of the wave fields emitted by this set of $m(m-1)/2$ smaller triangles, exploiting their similarity for acceleration of computation. A ray-tracing approach is applied for searching hidden triangles to express the occlusion effect. The final CGH is composed as an angular spectrum CGH and the FFT at the hologram plane is avoided by using a Fourier transform optical system for reconstruction. A fully analytical approach is proposed in [Liu et al. 2010], which expresses directly the complex amplitude at the hologram plane through the Fourier spectra of the wave fields emitted by the separate triangles in a triangular mesh model. Under certain approximations, the Fourier spectra relate the hologram plane to a specially devised frequency domain. They are found analytically by using a reference right triangle and the CGH is computed without FFT. A phase adjustment is made to avoid visualizing the edges of the triangular mesh in reconstruction due to the difference in the flat amplitude distributions in the triangles with abutting boundaries. Expressing the light beam emitted by an arbitrary triangle through transformation of a precalculated object beam emitted by a basic triangle is described in [Hosoyachi et al. 2013]. Calculation of the CGH there relies only on transformations in the spatial domain. Recording the basic beam on a plane requires a lot of memory due to the high density of fringes far away from the center of the plane. Its recording on a spherical surface is proposed to decrease the memory [Hosoyachi et al. 2013].

The issue of the expressiveness for the analytical or semi-analytical polygon-based approach is not as straightforward as for its numerical counterpart. First, analytical calculation of the angular spectra entails flat shading of the triangles in the 3D mesh and inevitable visualization of the mesh edges at reconstruction. Solution to this problem is proposed in [Park et al. 2015] by introducing a spatially varying amplitude in each triangle. Three different amplitude values are assigned to the vertices of a given triangle in accordance with the illumination direction and the normal vectors of the vertices that are provided by the used software for modeling the 3D object or through averaging the normal vectors to the plane of the neighboring triangles. The amplitude inside the triangle is found by an interpolation formula. Introduction of texture mapping to the fully analytical method is made in [Lim et al. 2013] by expanding the surface function inside the triangle into a Fourier series. The angular spectrum of the textured triangle is found as a weighted sum of analytically computed angular spectra with Fourier series coefficients as weights. The drawback is the significant amount of increase in computation time due to the requirement of taking many coefficients for better expressiveness. Holographic reconstruction from the textured polygon-based CGH is analyzed in [Lee et al. 2014] for improved semi-analytic approach. This is done by expressing the texture function as a Fourier series and composing a shift-invariant form for the textured angular spectrum at the hologram plane through some mathematical approximation of the formula for the angular spectrum of the unit amplitude triangle. This allows applying convolution and acceleration of computations. The drawback is reconstruction quality degradation for triangles highly inclined with respect to the hologram plane because of approximations [Lee et al. 2014]. The method is tested for the semi-analytic approach developed in [Kim et al. 2008a]. The semi-analytic algorithm for synthesis of the amplitude spectrum CGH for adaptive view direction change is further developed in [Cho et al. 2012]. Encoding of arbitrary angular reflectance distribution for the fully analytical approach is proposed in [Yeom and Park 2016] by relying on the fact that the angular spectra of a triangle in the global and local coordinate systems depend on the carrier wave or illumination direction. This is used to accumulate angular spectra of one and the same unit amplitude triangle corresponding to different carrier waves. Accumulation is based on a narrow diffraction angle around each carrier wave. Each angular spectrum is accumulated at a given diffracted intensity and a phase bias to compose the desired reflectance distribution. It is proved that it is possible to

introduce an approximated convolution approach, which avoids unnecessary separate computation of many spectra. In [Ji et al. 2016], a texture mapping method is developed without Fourier series expansion of the surface function, where each triangle is adaptively divided into smaller triangles with uniform amplitudes according to the texture mapping function. Similarity relations facilitate fast calculation of the angular spectra of the small triangles. Occlusion processing in the angular spectrum frequency domain for the fully analytical method is proposed in [Askari et al. 2017]. The occluded parts of the triangles are found by applying convolution in the hologram plane between the global angular spectrum of the rear triangles and the current triangle. The main advantage of the method is the convolution operation performed in the hologram plane. The result is blocking of the light waves from the rear triangles in the tilted planes of these triangles contrary to the silhouette mask approach that stops the light waves from the planes parallel to the hologram. This makes the method free from oblique angle artifacts [Askari et al. 2017].

3.3 Layer-based representation

The CGH synthesis can be highly accelerated by arranging the object data on planes. Such idea is implemented in [Bayraktar and Özcan 2010] by slicing a 3D object with a set of planar layers at equidistant depths parallel to the hologram plane. Each layer contains non-zero data for the visible object part and zeros for the invisible part (see Figure 7). The CGH is a sum of contributions from all layers obtained by using the Fresnel diffraction formula, convolution approach or ASM [Bayraktar and Özcan 2010; Trester 2000; Zhao et al. 2015]. CGH synthesis based on multiple fractional Fourier transforms is also proposed in [Zheng et al. 2009]. To obtain reconstruction quality close to that of the point cloud model, the number of layers should be rather large. Although the layer-based method has less computational complexity and operates with less amount of input data, its basic form can be applied only to diffusive Lambertian surfaces and provides a very narrow viewing zone around the viewing angle normal to the parallel layers.
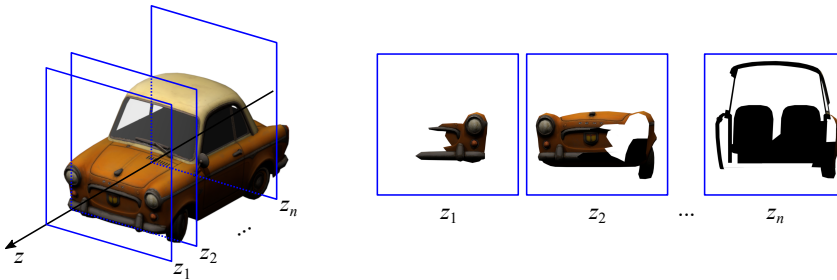

Fig. 7. Schematic representation of a layer-based CGH synthesis by cutting the 3D object with a set of planes parallel to the hologram plane and taking contribution from the visible parts of the object in each plane for a given viewing point.

To overcome the limitations in the basic implementation of the layer-based model, a multi-view layer-based CGH synthesis is proposed in [Chen et al. 2014]. The model is applied to the point cloud of a 3D object and a multiview rendering of the object is performed for fast computation of a full parallax CGH with occlusion and view-dependent shading. Accordingly, the point cloud is sliced with different set of layers for each viewing point. Angular tiling is used to display holograms calculated for the different viewpoints. The backward-forward propagation with a Ping-Pong algorithm [Dorsch et al. 1994] is used to deal with occlusions. In the first version of the developed algorithm, each considered point is projected to the nearest layer. For each layer, the diffraction pattern is calculated, and the patterns obtained for all layers are summed up in the

plane of the CGH. Optical reconstruction of points only on the layers creates a depth error for the objects points outside layers. This error is not expected to cause a serious degradation in the perceived reconstructed image, if the distance between consecutive layers is not more than the depth discrimination threshold of the HVS. An improved version of the method is proposed in [Chen and Chu 2015] by projecting the object point to the two closest layers located behind and in front of it with amplitude values determined by depth from defocus fused 3D method. Thus, the depth error is eliminated for observation direction coinciding with alignment direction of the layers, and the computation is four times faster [Chen and Chu 2015]. Composing a CGH from elemental holograms, which are calculated by the layer-based approach, is proposed in [Zhang et al. 2016a]. A separate set of planar layers is built within the viewing frustum of each elemental hologram. The so-called classification method for rapid sorting of points in a point cloud into the layers is introduced in [Su et al. 2016]. The sorting is made with an occlusion mask; the mask being filled with the points for the first layer is updated by removing the occluded points in the next layer and by adding all new points. A layer-based algorithm with rendering for a single viewpoint is developed in [Zhang et al. 2017] for synthesis of a 3D full parallax CGH with occlusion effects. A slab-based orthographic projection is used for slicing the 3D object. These projections are produced also between adjacent layers to create data for occlusion processing by performing silhouette mask culling for each layer. The complex wave field on each layer is propagated to hologram plane via ASM. Angular spectrum layer-based algorithm is used in [Zhao et al. 2016] to generate CGHs for layers at different depths. The CGHs are combined into groups to be exposed on the SLM by time-division multiplexing to increase the space-bandwidth product of reconstruction. In [Gilles et al. 2016], after slicing the 3D scene into layers parallel to the plane of the hologram, light is propagated from one layer to another. Shielding is performed using a point cloud approach and a threshold criterion to determine the number of points. The final CGH is obtained through propagation of the complex field on the layer nearest to the hologram. No visibility test is required for this technique to process occlusions. Fast computation of a CGH from a layer-based based model by using sparse FFT for calculation of diffraction is proposed in [Kim and Ro 2017]. Further development is proposed in [Jia et al. 2018] for the case of layers having a lot of zero-valued pixels due to occlusion effects. The developed two-step algorithm takes into consideration of only non-zero values and applies a sub-sparse 2D FFT calculation through performing two one-dimensional FFTs.

4 RAY-BASED CGH METHODS

Unlike wave-based techniques, the ray-based CGHs do not require knowledge about the geometric description of the scene. Instead, they rely solely on the captured intensity images of the scene under incoherent (white) light illumination. As incoherent holography approaches, the ray-based methods constitute an important category of CGH by enabling generation of holograms of still or dynamic real life scenes without requiring strict coherent illumination conditions and complex optical setups that should be immune to vibrations. Incoherent holography has also inspired some approaches in digital holography, such as optical scanning holography [T.-C. Poon et al. 1996] and Fresnel incoherent correlation holography [Rosen and Brooker 2007]. These methods utilize self-interference based and scanning based structured illumination techniques, respectively, which enable speckle free reconstructions [Liu et al. 2018]. Here we consider two categories of ray-based CGH methods, namely, HS and MVP holography, as incoherent holography techniques that utilize incoherently captured intensity images of the scenes in encoding the corresponding holograms.

4.1 Holographic stereogram

HSs can be either recorded optically by means of interference or calculated numerically. In both cases, the main ingredient is a set of multi-perspective images that define the information on the

hologram in hogel-by-hogel basis. Hogels can be interpreted as segments that are usually placed on a uniform rectangular grid and form the complete hologram when tiled. Historically, first optical implementations of the HS technique goes back to late 1960s [McCrickerd and George 1968]. In early 1970s, a set of perspective images calculated by a computer were used to record a HPO hologram by moving a vertical slit mask [King et al. 1970], i.e., the hogel for this HPO arrangement is a vertical segment that vertically covers the entire hologram. Yatagai first proposed computer synthesis of a HS in 1974 [Yatagai 1974], where each hogel was obtained through Fourier transform of a perspective projection of the 3D object. Verification of the concept was done for an object represented as a collection of many small flat surfaces and for a HPO hologram.

The set of multi-perspective images used in HS calculation corresponds to a set of rays that can be parametrized as a light field (LF). The ray optics formalism of the LF represents the light as a collection of rays. That is, at a given time, for a given wavelength, taking only the rays propagating in free space to, e.g., $+z$ direction, any ray can be parameterized by the four-dimensional (4D) LF $L(x, y, u, v)$ using the crossing points of rays on two parallel planes (x, y) and (u, v), respectively [Levoy 2006]. This so-called two-plane parametrization is depicted in Figure 8(a).
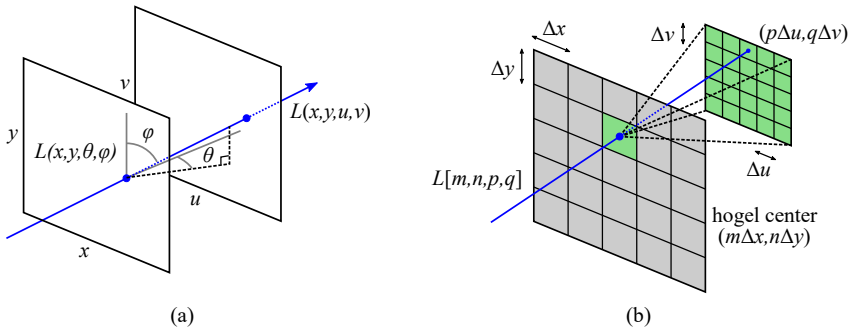

Fig. 8. 4D parametrization of the light field (a) and schematic representation of HS (b).

The two parallel planes can be directly linked to multi-perspective image capture setup by assigning (x, y) as the camera view plane and (u, v) as the image plane of the camera. The LF can be also equivalently represented by a space-angle parametrization $L(x, y, \theta, \phi)$ where θ and ϕ denote the propagation directions of the rays with respect to x and y axes, respectively. Thus, in either case, the (x, y) plane can be treated as the ray-sampling plane (RSP). The capture process involves two recording schemes. The first is recording of perspective projections of the scene from each spatial sampling point on the RSP with a setup consisting of usually a high number of low-resolution cameras. The second is recording of usually a smaller number of images with orthographic projection, i.e., capturing a set of parallel rays each of which corresponds to a different direction in the LF space-angle parametrization.

Let us consider the case illustrated in Figure 8(b), where the RSP coincides with the hologram plane and the HS is divided into a regular grid of hogels of size $\Delta x \times \Delta y$ with abutting boundaries. The corresponding captured discrete LF is denoted as $L[m, n, p, q] = L(m\Delta x, n\Delta y, p\Delta u, q\Delta v)$, where Δu and Δv are the pixel pitches of the captured intensity images. The HS then encodes the intensity

and directional information in the complex amplitude of the object field as

$$O_{HS}(x, y) = \sum_{m=1}^{M} \sum_{n=1}^{N} \text{rect}\left(\frac{x - m\Delta x}{\Delta x}\right) \text{rect}\left(\frac{y - n\Delta y}{\Delta y}\right) \tag{8}$$

$$\sum_{p=1}^{P} \sum_{q=1}^{Q} \sqrt{L[m, n, p, q]} \exp[j2\pi(f_x^{mnpq}x + f_y^{mnpq}y)],$$

where $(m\Delta x, n\Delta y)$ are the coordinates of the center of the hogel $[m, n]$ and (f_x^{mnpq}, f_y^{mnpq}) are the spatial frequency components for the ray $[m, n, p, q]$. According to the grating equation, for a reference plane wave incident normally to the plane of the hologram, the spatial frequencies for the ray $[m, n, p, q]$ are related to their angles of incidence with respect to (x, y) plane as

$$f_x^{mnpq} = \frac{\sin \theta_x^{mnpq}}{\lambda}, \quad f_y^{mnpq} = \frac{\sin \theta_y^{mnpq}}{\lambda} \tag{9}$$

As seen in Equation (8) and Equation (9), the diffractive properties of each hogel are determined by the encoded set of basis sinusoidal fringes with different amplitudes that reconstruct a set of plane waves propagating along a certain view angle in accordance with the spatial frequencies of the fringes [Halle et al. 1991; Lucente 1993, 1994]. The complex amplitude can, thus, be obtained by applying inverse Fourier transform to the captured images, which encodes intensity and directional information in the hogel. Such encoding scheme enables the calculation of CGH via FFT techniques, and thus, it significantly reduces the computation time of the CGH compared to wavefront-based approaches. However, this improvement in computation time comes at the expense of degradation in quality of the reconstructed images in comparison with the wavefront-based CGHs. The HS encoding corresponds to an approximation of the spherical wavefront due to a point source in the scene via a set of discontinuous planar patches, resulting in hogels with single complex exponential components that are unmatched in phase.
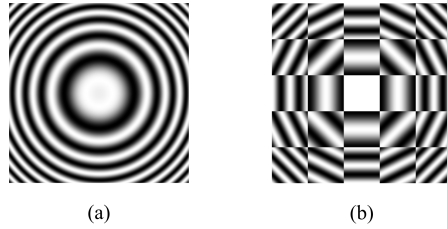

Fig. 9.   Real part of Fresnel diffraction kernel (a) and corresponding HS (b).

Figure 9 illustrates how HS approximates the Fresnel diffraction kernel for a point source. As mentioned in Section 3, PAS methods also approximate the wavefronts by using plane wave patches to take advantage of FFT in CGH calculation. In addition to that, however, the depth information of the scene is also used in those methods to match the phases of planar patches. This results in more accurate wave representation, and thus, higher quality reconstructed images. On the other hand, the HS approach is similar to image-order type of wavefront-based methods in the way of acquisition the scene data by capturing images of it. The CG rendering techniques are, thus, highly appropriate to include hidden surface removal, shading, reflections, texture, glossiness, mutual and self-occlusions in the encoded data for photorealistic reconstruction [Verma and Walia 2010].

The LF sampling setup in Figure 8(b) is impractical for real life scenes. It restricts the scene to be on either side of the hologram plane. The discrete LF $L[m, n, p, q]$ used for HS generation,
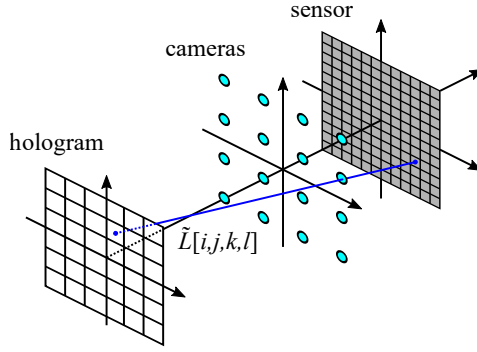
Fig. 10. LF sampling away from hologram plane by a set of cameras.

as in Equation (8), can be also acquired by capturing a set of 2D images at a certain distance from the hologram plane. As shown in Figure 10, the captured discrete LF can be parametrized as $\tilde{L}[i, j, k, l] = \tilde{L}(i\Delta\tilde{x}, j\Delta\tilde{y}, k\Delta\tilde{u}, l\Delta\tilde{v})$ by using another pair of parallel planes $(\tilde{x}, \tilde{y})$ and $(\tilde{u}, \tilde{v})$ with the former being the actual ray sampling plane on which the cameras are put. Each camera now captures different directional information for a given hogel and the pixels of each camera correspond to hogels, i.e., they sample the spatial information on the hologram plane. As usually there is no straightforward one-to-one correspondence between the samples of $L[m, n, p, q]$ and $\tilde{L}[i, j, k, l]$, it is necessary to resample $\tilde{L}[i, j, k, l]$ to obtain the desired ray samples $L[m, n, p, q]$ for CGH generation. By choosing the appropriate LF sampling parameters for the given scene, i.e., satisfying the prerequisites of the densely sampled LF, any ray is accurately obtained from the samples $\tilde{L}[i, j, k, l]$ via linear interpolation [Lin and Shum 2004]. This limits the disparity between adjacent views during capture such that it is within $[-1, 1]$ pixels with respect to hologram plane, thus restricting the distance between adjacent cameras and the boundaries of the captured scene. Such a framework ensures accurate resampling of $L[m, n, p, q]$ from $\tilde{L}[i, j, k, l]$.

A CGH generated as a HS possesses the main drawbacks of ray-based 3D light field displays. The image quality perceived from the reconstructed hologram is mainly determined by the spatio-angular resolution. The spatial sampling gives the perceived image resolution, whereas the angular sampling affects view-dependent image aspects such as motion parallax, specular reflection, occlusions, etc. The characteristics of the modulation transfer function allow analysis of optimum sampling of HS [Hilaire 1994]. The joint spatio-angular resolution of HS is dictated by the hogel size and it is subject to a trade-off due to the uncertainty principle inherent to diffraction. For improved spatial resolution, one needs to decrease the hogel size, which in turn degrades the angular resolution and vice versa. Besides that, to deliver the available angular resolution, the number of pixels within the hogels should be also sufficiently high. In practice, the characteristic of the HVS plays a key role in choosing the sampling parameters [Lucente 1994]. The lateral visual acuity of the HVS, when observing an object at distance d is given by

$$\Delta x^{HVS} = \frac{1.22\lambda d}{D_{eye}}, \tag{10}$$

where D_{eye} is the aperture size of the eye pupil [Goodman 1996]. That is, given an intended observation distance of the HS, the hogel size can be chosen to match with the HVS acuity. On the other hand, the pupil size of the eye puts an upper limit on the perceivable angular resolution as

$$\Delta\theta^{HVS} = 2\tan^{-1}\left(\frac{D_{eye}}{2d}\right), \tag{11}$$

which then can be also utilized to determine angular sampling (or spectral sampling of the fringes).

The HVS together with the depth range and the scene data impose strict requirements on the LF sampling. The LF capture for HS is usually required to be very dense with a high number of images at small parallax between neighboring views. The capture of real scenes needs a scanning camera positioned accurately at the viewpoints [Nikolskij et al. 2012]. Relieving the constraints can ease the capture process for HSs and enable using of multicamera systems instead of scanning camera rigs. The view synthesis and LF reconstruction algorithms are directly applicable in this context. In [Ohsawa et al. 2013], the amount of projections is reduced by using scene depth via shape-from-silhouette technique for a voxel-based model of the 3D object. A depth-corrected LF rendering is used in [Jurik et al. 2012] with a practical real scene capture setup. Reducing the number of captured images in [Hayashi et al. 2011; Kinoshita and Sakamoto 2009] involves ray interpolation by a distance transformation and light wave rotation. In [Sahin et al. 2016], an image based LF reconstruction with a Shearlet transform relieves the LF sampling requirement by a factor of up to 8×8, in the horizontal and vertical dimensions, without significant degradation in the perceived image quality.

Due to the LF sampling and diffraction from finite size hogels, objects far away from the hologram cannot be sharply reconstructed [Hilaire 1994; Wakunami and Yamaguchi 2011]. This makes HSs unsuitable for deep scenes. The concept of virtual light-ray sampling plane proposed in [Wakunami and Yamaguchi 2011; Yamaguchi 2013] reduces the blur from LF sampling. The resolution of reconstructed images for objects far away from the hologram plane is improved by hybrid computation of HS. This is achieved by i) locating a virtual plane close to the object and sampling the light rays from the object at this plane and ii) propagation of the complex amplitude from the virtual plane to the hologram using diffraction theory. The points in the virtual plane encode projection images produced by CG techniques as ray-tracing or image-based rendering. For encoding, each projection image is multiplied by a 2D random phase uniformly distributed in $[0, 2\pi]$ and Fourier transformed to obtain the complex amplitude in the virtual plane. Thus, the virtual plane contains an array of abutting elemental holograms. The complex amplitude in this plane is propagated by Fresnel diffraction to the CGH plane. Several virtual light-ray sampling planes can be introduced to reconstruct objects at different depths. The developed approach is used for multi-occlusion processing in [Wakunami et al. 2013] by locating virtual planes near the objects in the scene. Using the light-ray domain for occlusion processing allows development of a fast and simple algorithm. The proposed method with a virtual plane correctly represents mutual occlusion. In [Plesniak et al. 2006], the so-called reconfigurable image projection CGH is introduced by populating a virtual plane located at some distance from the hologram plane with projection primitives that create the desired distribution of the directional information. The virtual plane is sampled on a regular grid by hogels with abutting boundaries. For each hogel, the basis fringes on the hologram plane are found by Fresnel propagation. The resulting overlapping fringes on the hologram plane reduce artifacts caused by the discontinuity of the fringes at hogel boundaries in the conventional HS computing.

For high spatial and angular resolutions, the HS should consist of very small size of pixels, which can be provided by techniques such as lithography or HS printing. In printing, each hogel image is fed to an amplitude SLM that is focused on a silver-halide plate by a lens. A reference beam illuminates the plate from the opposite side, and a hogel is recorded as a volume reflection hologram. The average grain size of the available silver-halide emulsions can be as little as 10 nm. The HS printers can produce large size, high-quality, color HPO holograms [Brotherton-Ratcliffe et al. 2011]. When illuminated by a point source of white light, the printed HS spatially multiplexes the hogel images reconstructed from different hogels.

4.2 Multiple viewpoint projection holography

Similar to HS, the main motivation of MVP holography is the utilization of a set of 2D intensity images, captured under incoherent white light illumination, in CGH generation [Shaked et al. 2009]. A fundamental difference, however, is that MVP holograms aim at generating smooth (coherent) object wavefronts, in accordance with, e.g., Fourier or Fresnel hologram, which results in a different LF capture setup and problem formulation.
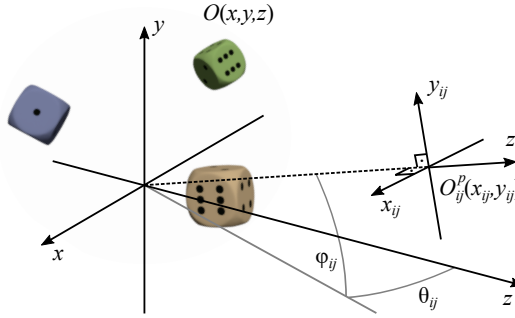

Fig. 11. LF capture geometry for MVP holography.

As illustrated in Figure 11, the LF capture setup in MVP holography involves a set of projection images $O_{ij}^p(x_{ij}, y_{ij})$ recorded from different angles (θ_{ij}, ϕ_{ij}). Those projection images actually correspond to orthogonal projections of the scene intensity function $O(x, y, z)$, which represents the light distribution that is assumed to be isotropically emitted from the surface of the objects in the scene, along the corresponding directions. That is,

$$O_{ij}^p(x_{ij}, y_{ij}) = \int O_{ij}(x_{ij}, y_{ij}, z_{ij}) dz_{ij}, \tag{12}$$

where $O_{ij}(x_{ij}, y_{ij}, z_{ij})$ is the representation of the scene intensity function with respect to the coordinates of the camera used for the projection along (θ_{ij}, ϕ_{ij}) [Sando et al. 2003]. One can rewrite Equation (12) by taking the 2D Fourier transform of both sides as

$$\tilde{O}_{ij}^p(u_{ij}, v_{ij}) = \iiint O_{ij}(x_{ij}, y_{ij}, z_{ij}) \exp\left[-j2\pi(u_{ij}x_{ij} + v_{ij}y_{ij})\right] dx_{ij}dy_{ij}dz_{ij}. \tag{13}$$

Under small-angle approximations, $\cos(\theta_{ij}) \approx 1$ and $\cos(\phi_{ij}) \approx 1$, these coefficients are shown to constitute a Fourier hologram of the scene $O(x, y, z)$ [Abookasis and Rosen 2003; Sando et al. 2003]. When an SLM is placed at the front focal plane of a lens and these complex-valued coefficients are properly coded and combined in a matrix to be fed to the SLM as real and nonnegative transmittance, a normally falling plane wave reconstructs the scene at the back focal plane of the lens.

The method in [Li et al. 2001] forms the complex-valued matrix from the data in the projection images captured at equal angular steps in a horizontal plane by a camera through an imaging lens. The function corresponds to the capture of a LF from a 3D object through a special optical system from two cylindrical lenses. Due to the HPO capability, however, defocused reconstructions are likely to occur normally to the recording axis. A full parallax system is proposed in [Abookasis and Rosen 2003] by acquisition of angular projections in a 2D grid and forming a 2D complex matrix. Each element of the matrix corresponds to a given viewpoint and the matrix is arranged in the order the projection images are captured. The Fourier hologram inherently includes the object field. Thus, having obtained the Fourier coefficients by Equation (13), other types of holograms such as Fresnel can be generated [Abookasis and Rosen 2006; Park et al. 2009; Sando et al. 2003], which enable

reconstruction without additional lenses. The full color reconstruction is demonstrated in [Sando et al. 2004] by building three CGHs for the primary colors. Analysis of different magnifications at three wavelengths is also provided. Different variations of the Fresnel hologram for short and long reconstruction distances are presented in [Abookasis and Rosen 2006]. Generation of Fourier and Fresnel holograms uses a slightly different projection geometry, where the image plane is fixed and thus not always normal to projection lines as in the conventional angular projection [Park et al. 2009]. The integral photography implemented in [Shaked et al. 2007] acquires projection images by a lens array. The projection images recorded by a digital camera are then used for a Fourier hologram.

Similar to HS, the main drawback of MVP holography is the need for capture of a large number of images with small angular increments in the projection angles, typically under 1 degree. Simultaneous capture of these images with a lenslet array is questionable because of the low resolution of the capture system [Ichihashi et al. 2012]. The number of projections is reduced in [Katz et al. 2007] and the intermediate projections are calculated by a view synthesis algorithm. The requirement for a distinct anchor point for interpolation of different perspectives entails increasing the number of the projections for textured and smooth scenes. Both anchor points and the number of projections must be chosen individually for each 3D object. Compressive sensing applied in [Brady et al. 2009; Rivenson et al. 2011] uses sparse representation of the input data in the Fourier space. That is, an under-sampled Fourier hologram is calculated from an undersampled set of projections. The Fourier space is non-uniformly sampled in such a way that the density of projections are kept higher in the central low frequency regions than in the high frequency regions. Two equations are built for reconstruction from the under-sampled Fourier hologram based on 2D-2D and 3D-2D reconstruction models. Successful 3D reconstructions are reported with only around 6% of all projections.

5 SPECKLE SUPPRESSION IN CGH

Holograms suffer from an inherent coherent imaging issue known as speckle noise. This issue is also relevant to CGHs and requires careful examination. In order to simulate diffused diffraction of light from the recorded scene and to avoid concentration of light on the CGH, usually random phases are added to the point sources of light (or equivalent primitives). As the image perceived by the HVS can be considered as a sum of point spread functions (PSF) corresponding to the scene points, the random phase added to the points causes random interference patterns, if the PSFs overlap on the retinal surface. This random interference is observed as random speckle patterns with high contrast and spatial frequency that heavily degrade the perceived quality. Thus, eliminating the speckle patterns from the holographic reconstructions is vital in order to achieve satisfactory visual quality.

Due to the different hologram generation in wavefront-based and ray-based CGH techniques, the speckle suppression methods differ in most cases and thus require separate examination for both CGH types. Some solutions, however, can be utilized in both cases as the speckle suppression is achieved through display technique means, i.e., by modifying the holographic display optics, rather than altering the hologram generation. Mostly these methods rely on reducing either the temporal or the spatial coherence of the reconstruction illumination. By using a diffuser, the spatial coherence of the light is decreased [Yamaguchi et al. 1994]. The temporal coherence is reduced by utilizing light-emitting diodes (LEDs) for illumination [Yaraş et al. 2009]. It should be noted, however, that the approaches reducing the coherence of the reconstruction light add blur to the reconstructed image, which can negatively affect the reproduction of deep scenes [Yaraş et al. 2009].

The amount of speckle noise in the reconstructed views is often evaluated as speckle contrast [Goodman 2007]. The contrast is obtained as the ratio of the standard deviation σ and mean of

the intensity values $\widehat{I}$ within the region of interest, i.e., $C = \sigma/\widehat{I}$. The region-of-interest should consist of uniform intensity values in view of the signal-dependent nature of the speckle noise. Subsequently, lower speckle contrast signifies better speckle suppression. Values equal to or under 0.05 are typically considered tolerable for sufficient image quality in laser projection displays. For high-end systems, however, achieving a more demanding speckle contrast criterion of 0.01 or less is recommended [Manni and Goodman 2012].

5.1 Speckle suppression methods for wavefront-based CGHs

One of the methods for suppressing speckle noise is to combine several CGH frames with statistically independent speckle patterns, which is known as random averaging [Amako et al. 1995]. The frames are displayed in sequence faster than the temporal response of the HVS, thus combining them in a time-multiplexed manner. As a result, the viewer perceives temporally averaged speckle patterns. The reduction at speckle contrast is proportional to $\sqrt{N}$ where N is the number of hologram frames. Thus, efficient speckle suppression requires a large number of frames, which in turn necessitates a high-speed display device to avoid separate frames to be resolved, as flickering, by the viewer.

As the random interference between the overlapping PSFs on the retina creates speckle noise, it can be suppressed by avoiding or reducing the overlaps. This can be achieved by generating several CGH frames, each including a subset of all the point sources, such that the distance between adjacent points separates the PSFs on the retina [Takaki and Yokouchi 2011]. The frames are then combined in a time-multiplexed manner in order to display them as a single reconstruction frame for the viewer with the entire set of point sources in the scene. The practical implementation of such speckle suppression in a holographic display can be accomplished by including a set of microlenses on the SLM, e.g., by using a digital micromirror device as in [Takaki and Yokouchi 2011]. In further studies, object point separation solution is adopted for lens-less holographic projection with undersampled bitmaps to generate the hologram [Makowski 2013]. To reduce the periodic interference due to the periodic locations of the separated object points, a random pixel separation method is proposed in [Mori et al. 2014]. By separating the points at random locations, the overlapping areas producing periodic interference are dispersed, thus reducing the overall unwanted interference. For polygon-based CGH methods, a time-multiplexing method incorporating angular spectrum interleaving reduces the speckle noise by a single carrier wave for each multiplexed CGH frame, which results in a linear phase distribution for the mesh surfaces, thus avoiding random interference [Ko and Park 2017]. Each frame produces speckle-free reconstructions, though time-multiplexing of multiple CGH frames is required in order to maintain the viewing angle supported by the hologram sampling size.

Similarly to point source separation applied in the object-oriented wavefront-based CGHs mentioned above, in image-oriented wavefront-based CGHs, speckle suppression can be achieved through ray separation. Based on the depth information, the utilized light rays can be separated into subsets of sparse rays, corresponding to sparse points in the scene [Utsugi and Yamaguchi 2014]. Due to finite angular resolution in ray casting, the view-dependent rays, which would correspond to a single point source, are usually mapped to multiple point sources. This issue is handled by quantizing the found point source locations on a uniform grid of voxels, resulting in pseudo-point sources. The time-multiplexed combination of CGHs for sparse subsets of rays results in reconstructions with reduced speckle. The reconstruction artifacts introduced in this approach due to ray quantization errors are addressed in [Mäkinen et al. 2018] by using the concept of densely sampled light field capture that enables accurate light ray resampling.

There also exist speckle suppression methods that do not rely on time-multiplexed reconstruction, but instead manage the speckle patterns without generating additional hologram frames through

various means. One of these methods achieves this for the display of phase-only holograms by cyclic sequential shifting of the hologram [Golan and Shoham 2009]. The deterministic shift-averaging method utilizes the properties of phase shifting in order to minimize the interference between different pairs of PSFs within certain squares of interest on the hologram. Based on the iterative Fourier transform algorithm (IFTA), the Fresnel ping-pong algorithm utilizes forward and backward propagation of the field between two different object planes along with amplitude adjustments in order to suppress speckles [Dorsch et al. 1994]. The method is modified in [Makowski et al. 2005] to accommodate phase-only CGHs by using two object planes with the hologram plane and intensity equalization to assure a phase-only CGH, while the amplitude adjustments reduce the speckle noise. An alternative solution for single frame speckle suppression replaces the use of random phase distribution and instead multiplies the object wave with virtual converging light [Shimobaba and Ito 2015]. For phase-only holographic displays, complex modulation is shown to reduce speckle noise without the need for iteration, thus making it suitable for improving image quality in dynamic displays [Qi et al. 2016].

Alternatives to random phase distribution are also proposed to avoid the generation of speckle patterns. In [Wyrowski and Bryngdahl 1989], an iterative Fourier-based algorithm is proposed for finding phase distributions eliminating the formation of speckle patterns. Similarly, by using an iterative optimization approach, object-dependent distributions is calculated [Bräuer et al. 1991]. In both cases, these distributions spread the light over a finite area in the Fourier domain, thus resulting in speckle-free diffraction patterns. Moreover, a deterministic method for object-independent phase distribution acquisition, which is mostly optimal for near constant magnitude objects, is reported. A quasi-band-limited distribution is also shown to be effective at recording Fourier transform holograms with reduces speckle [Yamaguchi et al. 1994].

5.2 Speckle suppression methods for ray-based CGHs

In the case of ray-based CGHs, random averaging is also applicable. In particular, different CGHs can be computed with a different sets of random phases and then they can be reconstructed in a time-multiplexed manner. However, the abovementioned point or light ray separation approaches are not directly applicable due to the requirement of explicit depth data of the scene. HSs can utilize a modified version of the pixel separation method. By separating the hogels on the hologram plane to different CGH frames, a time-multiplexed reconstruction of the hologram results in reduced interference between adjacent hogels [Makowski 2013; Takaki and Yokouchi 2011].

The interference patterns can be suppressed by phase modulation as proposed in [Takaki and Taira 2016]. The method transforms the speckle patterns into regular sinusoidal interference patterns with spatial frequency being higher than the cut-off spatial frequency of HVS. This is achieved by improving the viewing area continuity, i.e., the number of viewpoints is increased by generating virtual views between the originally captured views. As the lowest spatial frequency terms are generated by adjacent views, the analysis in [Takaki and Taira 2016] considers 2×2 views within the extent of the pupil, where the phases are set by modifying the coefficients of the intensity distribution on the retina. By maximizing certain coefficients, the spatial frequency is increased such that the human vision cut-off frequency is exceeded and the speckle patterns become invisible to the human eyes. Alternatively, the spatial bandwidth of the random phase distribution can be limited to reduce speckle noise [Takaki and Ikeda 2013]. Assuming a hologram pixel pitch of Δ and spatial bandwidth of B_p in the parallax images, the spatial bandwidth of the random phase distribution should be limited to $1/\Delta - B_p$ to ensure that the diffraction distribution is as uniform as possible and its deviation is minimized to avoid the generation of speckle noise.

6   CONCLUSIONS

This paper provides a survey of the state-of-the-art in the field of CGHs for 3D imaging. Development of methods for synthesis of such CGHs has shown steady growth over the last few decades due to the rapid progress in computing and optical devices for capture and visualization. In addition to dynamic optical reconstruction of such CGHs via advanced SLMs, it has become also possible to fabricate highly realistic CGHs on holographic plates. Especially for glasses-free visualization, there is still a big room for improvement in terms of optical devices to provide necessary size and bandwidth, i.e., space-bandwidth product. However, in the case of virtual or augmented reality type of visualization via near-eye or head-mounted display technology, the holographic imaging and in particular CGH based visualization is getting more close to "reality" due to significantly relieved requirements on the size and bandwidth of hologram compared to glasses-free display case.

Computation-wise, realistic representation of 3D objects sets extremely high demands in the CGH encoding process. The reason is the need for view-dependent full parallax rendering of information related to depth, color, texture, specular and diffuse reflection, mutual and self-occlusion, etc. The various 3D scene characteristics are supposed to be expressed as amplitude or phase variation within a CGH at different wavelengths. Complexity of rendered visual effects has a direct impact on the efficiency of the CGH computation, i.e., speed and memory usage. Fast generation methods are especially crucial for imaging of dynamic scenes. Thus, achieving better quality of reconstruction and acceleration of computation are the most up-to-date issues in the CGH synthesis.

The contemporary CGHs can be categorized into two broad categories as wavefront-based and ray-based methods depending mainly on the utilized object model and light propagation model. In both cases, the interference of the object and reference waves is computed, thus imitating the optical holographic recording. The wavefront-based methods rely on scalar diffraction in computing the object wave. The 3D object is modeled as a set of light primitives, which scatter light into wavefronts. The object wave is found by superposing such wavefronts. The amount of light primitives dictates the computational complexity. Point cloud model is the most computationally demanding approach, which represents a 3D object as a collection of point light sources. The great potential of this model for photorealistic imaging is the main motivation behind the numerous approaches proposed for acceleration of computation. The solutions make use of similarities in the Fresnel zone plates formed in the hologram by the point sources, which are located in a plane parallel to the hologram or on a line normal to the hologram, for creating look-up-tables. Other solutions exploit the small diffraction angle of the existing SLMs to restrict the contribution of a point source at the CGH plane or divide the hologram into elemental holograms, which allow for replacing the spherical wavefront from a point source by patches of plane waves. Acceleration can be also achieved by modeling the 3D objects as meshes of polygons or plane slices located at different depths parallel to hologram plane. The polygon-based method is more flexible in expressing object features, while the layer-based method is more computationally efficient. The numerical modification of the polygon-based method is well developed for incorporating texture, reflections, occlusions and other visual effects. Using a triangular mesh for 3D object representation offers an option for analytical computation at the expense of constraints set on the light field distribution within each triangle. Many efforts are focused on alleviation of these constraints. The narrow viewing zone is the main drawback of the layer-based approach. Overcoming this requires angular multiplexing of holograms corresponding to different viewing points. Due to assumption of independency between light primitives, parallel computing offers great potential in accelerating the computation of wavefront-based CGHs, which is extensively exploited in the literature. In summary, the current status of the wavefront-based CGHs can be described mainly as active development of better encoding algorithms. In the case of dynamic optical reconstruction, e.g., via SLMs, the pixel

pitch limits the bandwidth of CGH. Lithography or wavefront printing based methods enables visualization of static wavefront-based CGHs by means of a very fine resolution holographic plate and thus taking full advantage of highly realistic nature of such CGHs. Besides 3D imaging, another interesting application area of wavefront-based CGHs is holographic projection where CGHs are synthesized for 2D intensity images relying on Fresnel diffraction model. Holographic projection allows for lensless magnification.

The ray-based methods for CGH synthesis rely on acquiring spatial and angular intensity distribution of the propagating light rays, i.e., light field, due to given 3D object or scene. Encoding of this distribution can be based on the 2D images that are incoherently captured from different viewing points, which is a great advantage compared to wavefront-based methods in real life capture scenarios. Such multi-perspective images provide the light field as a collection of rays. CGH encoding follow two main schemes. The HS approach divides the hologram into holographic elements, which are called as hogels, and it encodes a set of fringes in each hogel, including a plane wave patch corresponding to each light field ray, based on the spatially and directionally varying intensity information in the captured light field. The HS is a significantly faster approach compared to wavefront-based CGHs, however it suffers from the spatio-angular resolution trade-off, which is dictated by the hogel size. The plane wave patches that are encoded incoherently in hogels are unmatched in phase along the hologram and this directly degrades the image quality for deep scenes compared to coherent case. An effective solution to this problem is achieved by the MVP approach, which makes it possible to reconstruct smooth wavefronts from a set of orthographic images. Other than dynamic optical reconstruction, the HS printing technology enables producing scalable static HSs. In summary, incoherent capture and fast computation are two important factors that make the ray-based methods attractive in creating dynamic or large size static holograms of real 3D scenes.

Speckle noise can significantly degrade reconstructed images in both ray-based and wave-based CGHs, which makes speckle suppression an important problem. Speckle suppression methods that are based on time-multiplexed computation (and reconstruction) of spatially separated object points or light rays demonstrate more effective implementations compared to the naive random (phase) averaging approach. However, there is still room for improvement in this problem.

ACKNOWLEDGMENTS

REFERENCES

David Abookasis and Joseph Rosen. 2003. Computer-generated holograms of three-dimensional objects synthesized from their multiple angular viewpoints. *J. Opt. Soc. Am. A* 20, 8 (Aug 2003), 1537–1545.

David Abookasis and Joseph Rosen. 2006. Three types of computer-generated hologram synthesized from multiple angular viewpoints of a three-dimensional scene. *Applied Optics* 45, 25 (Sep 2006), 6533–6538.

Lukas Ahrenberg, Philip Benzie, Marcus Magnor, and John Watson. 2006. Computer generated holography using parallel commodity graphics hardware. *Optics Express* 14, 17 (Aug 2006), 7636–7641.

Lukas Ahrenberg, Philip Benzie, Marcus Magnor, and John Watson. 2008. Computer generated holograms from three dimensional meshes using an analytic light transport model. *Applied Optics* 47, 10 (Apr 2008), 1567–1574.

Jun Amako, Hirotsuna Miura, and Tomio Sonehara. 1995. Speckle-noise reduction on kinoform reconstruction using a phase-only spatial light modulator. *Applied Optics* 34, 17 (Jun 1995), 3165–3171.

Daisuke Arai, Tomoyoshi Shimobaba, Takashi Nishitsuji, Takashi Kakue, Nobuyuki Masuda, and Tomoyoshi Ito. 2017. An accelerated hologram calculation using the wavefront recording plane method and wavelet transform. *Optics*

Communications 393 (2017), 107 − 112.

Mehdi Askari, Seong-Bok Kim, Kwang-Soo Shin, Seok-Bum Ko, Sang-Hoo Kim, Dae-Youl Park, Yeon-Gyeong Ju, and Jae-Hyeung Park. 2017. Occlusion handling using angular spectrum convolution in fully analytical mesh based computer generated hologram. *Optics Express* 25, 21 (Oct 2017), 25867–25878.

Muharrem Bayraktar and Meriç Özcan. 2010. Method to calculate the far field of three-dimensional objects for computer-generated holography. *Applied Optics* 49, 24 (Aug 2010), 4647–4654.

David Blinder and Peter Schelkens. 2018. Accelerated computer generated holography using sparse bases in the STFT domain. *Optics Express* 26, 2 (Jan 2018), 1461–1473.

Max Born. 1999. *Principles of Optics. Electromagnetic theory of propagation, interference and diffraction of light* (7. ed.). Cambridge University Press, Cambridge.

David J. Brady, Kerkil Choi, Daniel L. Marks, Ryoichi Horisaki, and Sehoon Lim. 2009. Compressive Holography. *Optics Express* 17, 15 (Jul 2009), 13040–13049.

Ralf Bräuer, Frank Wyrowski, and Olof Bryngdahl. 1991. Diffusers in digital holography. *J. Opt. Soc. Am. A* 8, 3 (Mar 1991), 572–578.

David C. Brotherton-Ratcliffe, Stanislovas J. Zacharovas, Ramunas J. Bakanas, Julius Pileckas, Andrej Nikolskij, and Jevgenij Kuchin. 2011. Digital holographic printing using pulsed RGB lasers. *Optical Engineering* 50 (2011), 50(9) 091307.

B. R. Brown and A. W. Lohmann. 1966. Complex Spatial Filtering with Binary Masks. *Applied Optics* 5, 6 (Jun 1966), 967–969.

Edward Buckley. 2011. Holographic Laser Projection. *J. Display Technol.* 7, 3 (Mar 2011), 135–140.

Jhen-Si Chen and Daping Chu. 2015. Improved layer-based method for rapid hologram generation and real-time interactive holographic display applications. *Optics Express* 23, 14 (Jul 2015), 18143–18155.

Jhen-Si Chen, Daping Chu, and Quinn Smithwick. 2014. Rapid hologram generation utilizing layer-based approach and graphic rendering for realistic three-dimensional image reconstruction by angular tiling. *Journal of Electronic Imaging* 23, 2 (2014), 023016–023016.

Rick H.-Y. Chen and Timothy D. Wilkinson. 2009. Computer generated hologram from point cloud using graphics processor. *Applied Optics* 48, 36 (Dec 2009), 6841–6850.

Jaebum Cho, Joonku Hahn, and Hwi Kim. 2012. Fast reconfiguration algorithm of computer generated holograms for adaptive view direction change in holographic three-dimensional display. *Optics Express* 20, 27 (Dec 2012), 28282–28291.

Jaebum Cho, Hwi Kim, Jiwoon Yeom, Gang Li, and Byoungho Lee. 2015. Rendering of reflective surfaces in polygon based computer generated holograms, In Imaging and Applied Optics 2015. *Imaging and Applied Optics 2015*, JT5A.21.

D. C. Chu, J. R. Fienup, and J. W. Goodman. 1973. Multiemulsion On-Axis Computer Generated Hologram. *Applied Optics* 12, 7 (Jul 1973), 1386–1388.

Giuseppe A. Cirino, Patrick Verdonck, Ronaldo D. Mansano, Jr. José C. Pizolato, Daniel B. Mazulquim, and Luiz G. Neto. 2011. Digital Holography: Computer-Generated Holograms and Diffractive Optics in Scalar Diffraction Domain.

Daniel Claus, Daciana Iliescu, and Peter Bryanston-Cross. 2011. Quantitative space-bandwidth product analysis in digital holography. *Applied Optics* 50, 34 (Dec 2011), H116–H127.

WJ Dallas. 1980. Computer-generated holograms. *The computer in optical research* 41 (1980), 291–366.

Xiao-Bin Dong, Seung-Cheol Kim, and Eun-Soo Kim. 2014a. MPEG-based novel look-up table for rapid generation of video holograms of fast-moving three-dimensional objects. *Optics Express* 22, 7 (Apr 2014), 8047–8067.

Xiao-Bin Dong, Seung-Cheol Kim, and Eun-Soo Kim. 2014b. Three-directional motion compensation-based novel-look-up-table for video hologram generation of three-dimensional objects freely maneuvering in space. *Optics Express* 22, 14 (Jul 2014), 16925–16944.

Rainer G. Dorsch, Adolf W. Lohmann, and Stefan Sinzinger. 1994. Fresnel ping-pong algorithm for two-plane computer-generated hologram display. *Applied Optics* 33, 5 (Feb 1994), 869–875.

Dennis Gabor. 1948. A New Microscopic Principle. *Nature* 161, 4098 (1948), 777–778.

R. W. Gerchberg and W. O. Saxton. 1972. Practical algorithm for determination of phase from image and diffraction plane pictures. *OPTIK* 35, 2 (1972), 237–&.

Antonin Gilles, Patrick Gioia, Rémi Cozot, and Luce Morin. 2016. Hybrid approach for fast occlusion processing in computer-generated hologram calculation. *Applied Optics* 55, 20 (Jul 2016), 5459–5470.

Lior Golan and Shy Shoham. 2009. Speckle elimination using shift-averaging in high-rate holographic projection. *Optics Express* 17, 3 (Feb 2009), 1330–1339.

Joseph W. Goodman. 1996. *Introduction to Fourier optics* (2nd., international ed.). McGraw-Hill, New York.

Joseph W. Goodman. 2007. *Speckle Phenomena in Optics: Theory and Applications.* Roberts and Company Publishers.

Michael W. Halle, Stephen A. Benton, Michael A. Klug, and John S. Underkoffler. 1991. Ultragram: a generalized holographic stereogram. In *Practical Holography V*, Vol. 1461. International Society for Optics and Photonics, 142–156.

Naotaka Hasegawa, Tomoyoshi Shimobaba, Takashi Kakue, and Tomoyoshi Ito. 2017. Acceleration of hologram generation by optimizing the arrangement of wavefront recording planes. *Applied Optics* 56, 1 (Jan 2017), A97–A103.

Noriyuki Hayashi, Yuji Sakamoto, and Yasuhiro Honda. 2011. Improvement of camera arrangement in computer-generated holograms synthesized from multi-view images. In *Proceedings of SPIE - The International Society for Optical Engineering*, Vol. 7957.

Pierre St Hilaire. 1994. Modulation transfer function and optimum sampling of holographic stereograms. *Applied Optics* 33, 5 (Feb 1994), 768–774.

Kohei Hosoyachi, Kazuhiro Yamaguchi, Tsubasa Ichikawa, and Yuji Sakamoto. 2013. Precalculation method using spherical basic object light for computer-generated hologram. *Applied Optics* 52, 1 (Jan 2013), A33–A44.

Yasuyuki Ichihashi, Ryutaro Oi, Takanori Senoh, Kenji Yamamoto, and Taiichiro Kurita. 2012. Real-time capture and reconstruction system with multiple GPUs for a 3D live scene by a generation from 4K IP images to 8K holograms. *Optics Express* 20, 19 (Sep 2012), 21645–21655.

Tsubasa Ichikawa, Yuji Sakamoto, Agus Subagyo, and Kazuhisa Sueoka. 2011. Calculation method of reflectance distributions for computer-generated holograms using the finite-difference time-domain method. *Applied Optics* 50, 34 (Dec 2011), H211–H219.

Tsubasa Ichikawa, Kazuhiro Yamaguchi, and Yuji Sakamoto. 2013a. Realistic expression for full-parallax computer-generated holograms with the ray-tracing method. *Applied Optics* 52, 1 (Jan 2013), A201–A209.

Tsubasa Ichikawa, Takuo Yoneyama, and Yuji Sakamoto. 2013b. CGH calculation with the ray tracing method for the Fourier transform optical system. *Optics Express* 21, 26 (Dec 2013), 32019–32031.

Shunsuke Igarashi, Tomoya Nakamura, Kyoji Matsushima, and Masahiro Yamaguchi. 2018. Efficient tiled calculation of over-10-gigapixel holograms using ray-wavefront conversion. *Optics Express* 26, 8 (Apr 2018), 10773–10786.

Dajeong Im, Jaebum Cho, Joonku Hahn, Byoungho Lee, and Hwi Kim. 2015. Accelerated synthesis algorithm of polygon computer-generated holograms. *Optics Express* 23, 3 (Feb 2015), 2863–2871.

Boaz Jessie Jackin, Shinpei Watanabe, Kanemitsu Ootsu, Takeshi Ohkawa, Takashi Yokota, Yoshio Hayasaki, Toyohiko Yatagai, and Takanobu Baba. 2018. Decomposition method for fast computation of gigapixel-sized Fresnel holograms on a graphics processing unit cluster. *Applied Optics* 57, 12 (Apr 2018), 3134–3145.

Yeong-Min Ji, Hanju-Yeom, and Jae-Hyeung Park. 2016. Efficient texture mapping by adaptive mesh division in mesh-based computer generated hologram. *Optics Express* 24, 24 (Nov 2016), 28154–28169.

Jia Jia, Juan Liu, Guofan Jin, and Yongtian Wang. 2014. Fast and effective occlusion culling for 3D holographic displays by inverse orthographic projection with low angular sampling. *Applied Optics* 53, 27 (Sep 2014), 6287–6293.

Jia Jia, Jhen Si, and Daping Chu. 2018. Fast two-step layer-based method for computer generated hologram using sub-sparse 2D fast Fourier transform. *Optics Express* 26, 13 (Jun 2018), 17487–17497.

Jia Jia, Yongtian Wang, Juan Liu, Xin Li, Yijie Pan, Zhumei Sun, Bin Zhang, Qing Zhao, and Wei Jiang. 2013. Reducing the memory usage for effectivecomputer-generated hologram calculation using compressed look-up table in full-color holographic display. *Applied Optics* 52, 7 (Mar 2013), 1404–1412.

Shuming Jiao, Zhaoyong Zhuang, and Wenbin Zou. 2017. Fast computer generated hologram calculation with a mini look-up table incorporated with radial symmetric interpolation. *Optics Express* 25, 1 (Jan 2017), 112–123.

J. L. Juárez-Pérez, A. Olivares-Pérez, and L. R. Berriel-Valdos. 1997. Nonredundant calculations for creating digital Fresnel holograms. *Applied Optics* 36, 29 (Oct 1997), 7437–7443.

Joel Jurik, Thomas Burnett, Michael Klug, and Paul Debevec. 2012. Geometry-corrected light field rendering for creating a holographic stereogram. In *2012 IEEE Computer Society Conference on Computer Vision and Pattern Recognition Workshops*. 9–13.

Hoonjong Kang, Tomohiko Fujii, Takeshi Yamaguchi, and Hiroshi Yoshikawa. 2007. Compensated phase-added stereogram for real-time holographic display. *Optical Engineering* 46 (2007), 095802 – 0958011.

Hoonjong Kang, Elena Stoykova, Youngmin Kim, Sunghee Hong, Joosup Park, and Jisoo Hong. 2016b. Color Holographic Wavefront Printing Technique for Realistic Representation. *IEEE Transactions on Industrial Informatics* 12, 4 (2016), 1590–1598.

Hoonjong Kang, Elena Stoykova, and Hiroshi Yoshikawa. 2016a. Fast phase-added stereogram algorithm for generation of photorealistic 3D content. *Applied Optics* 55, 3 (Jan 2016), A135–A143.

Hoonjong Kang, Takeshi Yamaguchi, and Hiroshi Yoshikawa. 2008a. Accurate phase-added stereogram to improve the coherent stereogram. *Applied Optics* 47, 19 (Jul 2008), D44–D54.

Hoonjong Kang, Takeshi Yamaguchi, Hiroshi Yoshikawa, Seung-Cheol Kim, and Eun-Soo Kim. 2008b. Acceleration method of computing a compensated phase-added stereogram on a graphic processing unit. *Applied Optics* 47, 31 (Nov 2008), 5784–5789.

Barak Katz, Natan T. Shaked, and Joseph Rosen. 2007. Synthesizing computer generated holograms with reduced number of perspective projections. *Optics Express* 15, 20 (Oct 2007), 13250–13255.

Hwi Kim, Joonku Hahn, and Byoungho Lee. 2008a. Mathematical modeling of triangle-mesh-modeled three-dimensional surface objects for digital holography. *Applied Optics* 47, 19 (Jul 2008), D117–D127.

Hak Gu Kim and Yong Man Ro. 2017. Ultrafast layer based computer-generated hologram calculation with sparse template holographic fringe pattern for 3-D object. *Optics Express* 25, 24 (Nov 2017), 30418–30427.

Myung K. Kim. 2011. *Digital Holographic Microscopy : Principles, Techniques, and Applications.* Springer New York, New York.

Seung-Cheol Kim, Xiao-Bin Dong, and Eun-Soo Kim. 2015. Accelerated one-step generation of full-color holographic videos using a color-tunable novel-look-up-table method for holographic three-dimensional television broadcasting. *Scientific Reports* 5, 1 (2015), 14056.

Seung-Cheol Kim, Xiao-Bin Dong, Min-Woo Kwon, and Eun-Soo Kim. 2013. Fast generation of video holograms of three-dimensional moving objects using a motion compensation-based novel look-up table. *Optics Express* 21, 9 (May 2013), 11568–11584.

Seung-Cheol Kim and Eun-Soo Kim. 2008. Effective generation of digital holograms of three-dimensional objects using a novel look-up table method. *Applied Optics* 47, 19 (Jul 2008), D55–D62.

Seung-Cheol Kim, Jae-Man Kim, and Eun-Soo Kim. 2012. Effective memory reduction of the novel look-up table with one-dimensional sub-principle fringe patterns in computer-generated holograms. *Optics Express* 20, 11 (May 2012), 12021–12034.

Seung-Cheol Kim, Jung-Hoon Yoon, and Eun-Soo Kim. 2008b. Fast generation of three-dimensional video holograms by combined use of data compression and lookup table techniques. *Applied Optics* 47, 32 (Nov 2008), 5986–5995.

M. C. King, A. M. Noll, and D. H. Berry. 1970. A New Approach to Computer-Generated Holography. *Applied Optics* 9, 2 (Feb 1970), 471–475.

M. Kinoshita and Y. Sakamoto. 2009. Computer-generated holograms at an arbitrary viewpoint synthesized from multi-view images. *Proc. SPIE* 7233, 72330Z.

Seok-Beom Ko and Jae-Hyeung Park. 2017. Speckle reduction using angular spectrum interleaving for triangular mesh based computer generated hologram. *Optics Express* 25, 24 (Nov 2017), 29788–29797.

Min-Woo Kwon, Seung-Cheol Kim, and Eun-Soo Kim. 2016. Three-directional motion-compensation mask-based novel look-up table on graphics processing units for video-rate generation of digital holographic videos of three-dimensional scenes. *Applied Optics* 55, 3 (Jan 2016), A22–A31.

Douglas Lanman, Ramesh Raskar, and Gabriel Taubin. 2008. Modeling and Synthesis of Aperture Effects in Cameras. In *Computational Aesthetics in Graphics, Visualization, and Imaging.* The Eurographics Association, 81–88.

Seok Lee, Hyunsung Chang, Hocheon Wey, and Dongkyung Nam. 2016. Sampling and error analysis of radial symmetric interpolation for fast hologram generation. *Applied Optics* 55, 3 (Jan 2016), A104–A110.

Wooyoung Lee, Dajeong Im, Jeongyeup Paek, Joonku Hahn, and Hwi Kim. 2014. Semi-analytic texturing algorithm for polygon computer-generated holograms. *Optics Express* 22, 25 (Dec 2014), 31180–31191.

Emmett N. Leith and Juris Upatnieks. 1962. Reconstructed Wavefronts and Communication Theory. *J. Opt. Soc. Am.* 52, 10 (Oct 1962), 1123–1130.

Detlef Leseberg and Christian Frère. 1988. Computer-generated holograms of 3-D objects composed of tilted planar segments. *Applied Optics* 27, 14 (Jul 1988), 3020–3024.

Mark Levoy. 2006. Light Fields and Computational Imaging. *Computer* 39, 8 (2006), 46–55.

Youzhi Li, David Abookasis, and Joseph Rosen. 2001. Computer-generated holograms of three-dimensional realistic objects recorded without wave interference. *Applied Optics* 40, 17 (Jun 2001), 2864–2870.

Hong-Gi Lim, Na-Young Jo, and Jae-Hyeung Park. 2013. Hologram synthesis with fast texture update of triangular meshes, In Digital Holography and Three-Dimensional Imaging. *Digital Holography and Three-Dimensional Imaging*, DW2A.8.

Zhouchen Lin and Heung-Yeung Shum. 2004. A Geometric Analysis of Light Field Rendering. *International Journal of Computer Vision* 58, 2 (2004), 121–138.

Jung-Ping Liu, Wang-Yu Hsieh, Ting-Chung Poon, and Peter Tsang. 2011. Complex Fresnel hologram display using a single SLM. *Applied Optics* 50, 34 (Dec 2011), H128–H135.

Jung-Ping Liu, Tatsuki Tahara, Yoshio Hayasaki, and Ting-Chung Poon. 2018. Incoherent Digital Holography: A Review. *Applied Sciences* 8 (01 2018), 143.

Yuan-Zhi Liu, Jian-Wen Dong, Yi-Ying Pu, Bing-Chu Chen, He-Xiang He, and He-Zhou Wang. 2010. High-speed full analytical holographic computations for true-life scenes. *Optics Express* 18, 4 (Feb 2010), 3345–3351.

Adolf W. Lohmann, Rainer G. Dorsch, David Mendlovic, Zeev Zalevsky, and Carlos Ferreira. 1996. Space–bandwidth product of optical signals and systems. *J. Opt. Soc. Am. A* 13, 3 (Mar 1996), 470–473.

A. W. Lohmann and D. P. Paris. 1967. Binary Fraunhofer Holograms, Generated by Computer. *Applied Optics* 6, 10 (Oct 1967), 1739–1748.

Mark E. Lucente. 1993. Interactive computation of holograms using a look-up table. *Journal of Electronic Imaging* 2, 1 (1993), 28–34.

Mark E. Lucente. 1994. *Diffraction-specific Fringe Computation for Electro-holography.* Ph.D. Dissertation. Cambridge, MA, USA.

Andrew Maimone, Andreas Georgiou, and Joel S. Kollin. 2017. Holographic Near-eye Displays for Virtual and Augmented Reality. *ACM Trans. Graph.* 36, 4, Article 85 (July 2017), 16 pages.

Jani Mäkinen, Erdem Sahin, and Atanas Gotchev. 2018. Speckle reduction method for image-based coherent stereogram generation. *Optics Express* 26, 5 (Mar 2018), 5381–5394.

Michał Makowski. 2013. Minimized speckle noise in lens-less holographic projection by pixel separation. *Optics Express* 21, 24 (Dec 2013), 29205–29216.

Michał Makowski, Maciej Sypek, Andrzej Kolodziejczyk, and Grzegorz Mikuła. 2005. Three-plane phase-only computer hologram generated with iterative Fresnel algorithm. *Optical Engineering* 44, 12 (2005), 125805.

Jeffrey G. Manni and Joseph W. Goodman. 2012. Versatile method for achieving 1% speckle contrast in large-venue laser projection displays using a stationary multimode optical fiber. *Optics Express* 20, 10 (May 2012), 11288–11315.

Kyoji Matsushima. 2005a. Computer-generated holograms for three-dimensional surface objects with shade and texture. *Applied Optics* 44, 22 (Aug 2005), 4607–4614.

Kyoji Matsushima. 2005b. Exact hidden-surface removal in digitally synthetic full-parallax holograms, In Practical Holography XIX: Materials and Applications. *Proc. SPIE* 5742, 25–32.

Kyoji Matsushima. 2006. Performance of the polygon-source method for creating computer-generated holograms of surface objects. In *Proceedings of ICO Topical Meeting on Optoinformatics/Information Photonics*. 99–100.

Kyoji Matsushima. 2008. Formulation of the rotational transformation of wave fields and their application to digital holography. *Applied Optics* 47, 19 (Jul 2008), D110–D116.

Kyoji Matsushima and Sumio Nakahara. 2009. Extremely high-definition full-parallax computer-generated hologram created by the polygon-based method. *Applied Optics* 48, 34 (Dec 2009), H54–H63.

Kyoji Matsushima, Masaki Nakamura, and Sumio Nakahara. 2014. Silhouette method for hidden surface removal in computer holography and its acceleration using the switch-back technique. *Optics Express* 22, 20 (Oct 2014), 24450–24465.

Kyoji Matsushima, Hagen Schimmel, and Frank Wyrowski. 2003. Fast calculation method for optical diffraction on tilted planes by use of the angular spectrum of plane waves. *J. Opt. Soc. Am. A* 20, 9 (Sep 2003), 1755–1762.

Kyoji Matsushima and Noriaki Sonobe. 2018. Full-color digitized holography for large-scale holographic 3D imaging of physical and nonphysical objects. *Applied Optics* 57, 1 (Jan 2018), A150–A156.

Kyoji Matsushima and Masahiro Takai. 2000. Recurrence formulas for fast creation of synthetic three-dimensional holograms. *Applied Optics* 39, 35 (Dec 2000), 6587–6594.

J. T. McCrickerd and Nicholas George. 1968. Holographic stereogram from sequential component photographs. *Applied Physics Letters* 12, 1 (1968), 10–12.

Yutaka Mori, Takahiko Fukuoka, and Takanori Nomura. 2014. Speckle reduction in holographic projection by random pixel separation with time multiplexing. *Applied Optics* 53, 35 (Dec 2014), 8182–8188.

Andrej Nikolskij, David C. Brotherton-Ratcliffe, Ramunas Bakanas, Stanislovas Zacharovas, and Julius Pileckas. 2012. Image capture system for a digital holographic printer.

Hirohito Nishi, Kyoji Matsushima, and Sumio Nakahara. 2011. Rendering of specular surfaces in polygon-based computer-generated holograms. *Applied Optics* 50, 34 (Dec 2011), H245–H252.

Takashi Nishitsuji, Tomoyoshi Shimobaba, Takashi Kakue, and Tomoyoshi Ito. 2015. Fast calculation of computer-generated hologram using run-length encoding based recurrence relation. *Optics Express* 23, 8 (Apr 2015), 9852–9857.

Takashi Nishitsuji, Tomoyoshi Shimobaba, Takashi Kakue, Nobuyuki Masuda, and Tomoyoshi Ito. 2012. Fast calculation of computer-generated hologram using the circular symmetry of zone plates. *Optics Express* 20, 25 (Dec 2012), 27496–27502.

Yusuke Ohsawa, Kazuhiro Yamaguchi, Tsubasa Ichikawa, and Yuji Sakamoto. 2013. Computer-generated holograms using multiview images captured by a small number of sparsely arranged cameras. *Applied Optics* 52, 1 (Jan 2013), A167–A176.

Naohisa Okada, Tomoyoshi Shimobaba, Yasuyuki Ichihashi, Ryutaro Oi, Kenji Yamamoto, Takashi Kakue, and Tomoyoshi Ito. 2014. Fast calculation of a computer-generated hologram for RGB and depth images using a Wavefront recording plane method. *Photonics Letters of Poland* 6, 3 (2014), 90–92.

N. Padmanaban, Y. Peng, and G. Wetzstein. 2019. Holographic Near-Eye Displays Based on Overlap-Add Stereograms. *ACM Trans. Graph. (SIGGRAPH Asia)* 6 (2019). Issue 38.

Yijie Pan, Yongtian Wang, Juan Liu, Xin Li, and Jia Jia. 2013. Fast polygon-based method for calculating computer-generated holograms in three-dimensional display. *Applied Optics* 52, 1 (Jan 2013), A290–A299.

Yuechao Pan, Xuewu xu, Sanjeev Solanki, Xinan Liang, Ridwan Bin Adrian Tanjung, Chiwei Tan, and Tow-Chong Chong. 2009. Fast CGH computation using S-LUT on GPU. *Optics Express* 17 (10 2009), 18543–18555.

Jae-Hyeung Park. 2017. Recent progress in computer-generated holography for three-dimensional scenes. *Journal of Information Display* 18, 1 (2017), 1–12.

Jae-Hyeung Park, Min-Su Kim, Ganbat Baasantseren, and Nam Kim. 2009. Fresnel and Fourier hologram generation using orthographic projection images. *Optics Express* 17, 8 (Apr 2009), 6320–6334.

Jae-Hyeung Park, Seong-Bok Kim, Han-Ju Yeom, Hee-Jae Kim, HuiJun Zhang, BoNi Li, Yeong-Min Ji, Sang-Hoo Kim, and Seok-Bum Ko. 2015. Continuous shading and its fast update in fully analytic triangular-mesh-based computer generated

hologram. *Optics Express* 23, 26 (Dec 2015), 33893–33901.

Anh-Hoang Phan, Md A. Alam, Seok-Hee Jeon, Jeong-Hyeon Lee, and Nam Kim. 2014. Fast hologram generation of long-depth object using multiple wavefront recording planes. *Proc. SPIE* 9006, 900612.

Wendy J. Plesniak, Michael W. Halle, V. Michael Bove, James Barabas, and Ravikanth Pappu. 2006. Reconfigurable image projection holograms. *Optical Engineering* 45, 11 (2006), 115801.

Ting-Chung Poon and Jung-Ping Liu. 2014. *Introduction to Modern Digital Holography with MATLAB*.

Yijun Qi, Chenliang Chang, and Jun Xia. 2016. Speckleless holographic display by complex modulation based on double-phase method. *Optics Express* 24, 26 (Dec 2016), 30368–30378.

Yair Rivenson, Adrian Stern, and Joseph Rosen. 2011. Compressive multiple view projection incoherent holography. *Optics Express* 19, 7 (Mar 2011), 6109–6118.

Joseph Rosen and Gary Brooker. 2007. Digital spatially incoherent Fresnel holography. *Optics Letters* 32, 8 (Apr 2007), 912–914.

Erdem Sahin, Suren Vagharshakyan, Jani Mäkinen, Robert Bregovic, and Atanas Gotchev. 2016. Shearlet-domain light field reconstruction for holographic stereogram generation. In *2016 IEEE International Conference on Image Processing (ICIP)*. 1479–1483.

Yusuke Sando, Masahide Itoh, and Toyohiko Yatagai. 2003. Holographic three-dimensional display synthesized from three-dimensional Fourier spectra of real existing objects. *Optics Letters* 28, 24 (Dec 2003), 2518–2520.

Yusuke Sando, Masahide Itoh, and Toyohiko Yatagai. 2004. Color computer-generated holograms from projection images. *Optics Express* 12, 11 (May 2004), 2487–2493.

Natan T. Shaked, Barak Katz, and Joseph Rosen. 2009. Review of three-dimensional holographic imaging by multiple-viewpoint-projection based methods. *Applied Optics* 48, 34 (Dec 2009), H120–H136.

Natan T. Shaked, Joseph Rosen, and Adrian Stern. 2007. Integral holography: white-light single-shot hologram acquisition. *Optics Express* 15, 9 (Apr 2007), 5754–5760.

Tomoyoshi Shimobaba and Tomoyoshi Ito. 2015. Random phase-free computer-generated hologram. *Optics Express* 23, 7 (Apr 2015), 9549–9554.

Tomoyoshi Shimobaba and Tomoyoshi Ito. 2017. Fast generation of computer-generated holograms using wavelet shrinkage. *Optics Express* 25, 1 (Jan 2017), 77–87.

Tomoyoshi Shimobaba, Tomoyoshi Ito, Nobuyuki Masuda, Yasuyuki Ichihashi, and Naoki Takada. 2010. Fast calculation of computer-generated-hologram on AMD HD5000 series GPU and OpenCL. *Optics Express* 18, 10 (May 2010), 9955–9960.

Tomoyoshi Shimobaba, Nobuyuki Masuda, and Tomoyoshi Ito. 2009. Simple and fast calculation algorithm for computer-generated hologram with wavefront recording plane. *Optics Letters* 34, 20 (Oct 2009), 3133–3135.

Quinn Y. J. Smithwick, James Barabas, Daniel E. Smalley, and V. Michael Bove. 2010. Interactive holographic stereograms with accommodation cues. *Proc.SPIE* 7619, 761903–7619013.

Pierre St-Hilaire, Stephen A. Benton, Mark E. Lucente, Mary Lou Jepsen, J. Kollin, Hiroshi Yoshikawa, and John S. Underkoffler. 1990. Electronic display system for computational holography. In *Practical Holography IV*, Stephen A. Benton (Ed.), Vol. 1212. International Society for Optics and Photonics, SPIE, 174 – 182.

Elena Stoykova, Fahri Yaraş, Ali Özgür Yontem, Hoonjong Kang, Levent Onural, Philippe Hamel, Yves Delacrétaz, Isabelle Bergoënd, Cristian Arfire, and Christian Depeursinge. 2013. Optical reconstruction of transparent objects with phase-only SLMs. *Optics Express* 21, 23 (Nov 2013), 28246–28257.

Ping Su, Wenbo Cao, Jianshe Ma, Bingchao Cheng, Xianting Liang, Liangcai Cao, and Guofan Jin. 2016. Fast Computer-Generated Hologram Generation Method for Three-Dimensional Point Cloud Model. *Journal of Display Technology* 12, 12 (2016), 1688–1694.

Athanasia Symeonidou, David Blinder, Adrian Munteanu, and Peter Schelkens. 2015. Computer-generated holograms by multiple wavefront recording plane method with occlusion culling. *Optics Express* 23, 17 (Aug 2015), 22149–22161.

Athanasia Symeonidou, David Blinder, and Peter Schelkens. 2018. Colour computer-generated holography for point clouds utilizing the Phong illumination model. *Optics Express* 26, 8 (Apr 2018), 10282–10298.

T.-C. Poon, M. H. Wu, K. Shinoda, and Y. Suzuki. 1996. Optical scanning holography. *Proc. IEEE* 84, 5 (1996), 753–764.

Yasuhiro Takaki and Kyohei Ikeda. 2013. Simplified calculation method for computer-generated holographic stereograms from multi-view images. *Optics Express* 21, 8 (Apr 2013), 9652–9663.

Yasuhiro Takaki and Nichiyo Nago. 2010. Multi-projection of lenticular displays to construct a 256-view super multi-view display. *Optics Express* 18, 9 (Apr 2010), 8824–8835.

Yasuhiro Takaki and Kengo Taira. 2016. Speckle regularization and miniaturization of computer-generated holographic stereograms. *Optics Express* 24, 6 (Mar 2016), 6328–6340.

Yasuhiro Takaki and Masahito Yokouchi. 2011. Speckle-free and grayscale hologram reconstruction using time-multiplexing technique. *Optics Express* 19, 8 (2011), 7567–7579.

Tullio Tommasi and Bruno Bianco. 1993. Computer-generated holograms of tilted planes by a spatial frequency approach. *J. Opt. Soc. Am. A* 10, 2 (Feb 1993), 299–305.

Seymour Trester. 2000. Computer-simulated Fresnel holography. *European Journal of Physics* 21, 4 (2000), 317–331.

P. W. M. Tsang, K. W. K. Cheung, and T.-C. Poon. 2012. Real-time relighting of digital holograms based on wavefront recording plane method. *Optics Express* 20, 6 (Mar 2012), 5962–5967.

P. W. M. Tsang, Y. T. Chow, and T.-C. Poon. 2016. Generation of complementary sampled phase-only holograms. *Opt. Express* 24, 20 (Oct 2016), 23390–23395.

P. W. M. Tsang, Y. T. Chow, and T.-C. Poon. 2017. Generation of patterned-phase-only holograms (PPOHs). *Opt. Express* 25, 8 (Apr 2017), 9088–9093.

P. W. M. Tsang and T.-C. Poon. 2015. Fast generation of digital holograms based on warping of the wavefront recording plane. *Optics Express* 23, 6 (Mar 2015), 7667–7673.

P. W. M. Tsang and T.-C. Poon. 2016. Review on the state-of-the-art technologies for acquisition and display of digital holograms. *IEEE Trans. Industrial Informatics* 12, 3 (June 2016), 886– 901.

P. W. M. Tsang, T.-C. Poon, and Y. M. Wu. 2018. Review of fast methods for point-based computer-generated holography [Invited]. *Photonics Research* 6, 9 (Sep 2018), 837–846.

Raul Tudela, Ignasi Labastida, Estela Martin-Badosa, Santiago Vallmitjana, Ignacio Juvells, and Artur Carnicer. 2002. A simple method for displaying Fresnel holograms on liquid crystal panels. *Optics Communications* 214, 1 (2002), 107–114.

Takeru Utsugi and Masahiro Yamaguchi. 2014. Speckle-suppression in hologram calculation using ray-sampling plane. *Optics Express* 22, 14 (Jul 2014), 17193–17206.

E. G. van Putten, I. M. Vellekoop, and A. P. Mosk. 2008. Spatial amplitude and phase modulation using commercial twisted nematic LCDs. *Appl. Opt.* 47, 12 (Apr 2008), 2076–2081.

Vishal Verma and Ekta Walia. 2010. 3D Rendering - Techniques and challenges. *International Journal of Engineering and Technology* 2, 2 (2010), 29–33.

Koki Wakunami and Masahiro Yamaguchi. 2011. Calculation for computer generated hologram using ray-sampling plane. *Optics Express* 19, 10 (May 2011), 9086–9101.

Koki Wakunami, Hiroaki Yamashita, and Masahiro Yamaguchi. 2013. Occlusion culling for computer generated hologram based on ray-wavefront conversion. *Optics Express* 21, 19 (Sep 2013), 21811–21822.

James P. Waters. 1966. Holographic image synthesis utilizing theoretical methods. *Applied Physics Letters* 9, 11 (1966), 405–407.

Hui Wei, Guanghong Gong, and Ni Li. 2016. Improved look-up table method of computer-generated holograms. *Applied Optics* 55, 32 (Nov 2016), 9255–9264.

Jiantong Weng, Tomoyoshi Shimobaba, Naohisa Okada, Hirotaka Nakayama, Minoru Oikawa, Nobuyuki Masuda, and Tomoyoshi Ito. 2012. Generation of real-time large computer generated hologram using wavefront recording method. *Optics Express* 20, 4 (Feb 2012), 4018–4023.

Gordon Wetzstein, Douglas Lanman, Matthew Hirsch, and Ramesh Raskar. 2012. Tensor Displays: Compressive Light Field Synthesis Using Multilayer Displays with Directional Backlighting. *ACM Trans. Graph.* 31, 4, Article 80 (July 2012), 11 pages.

Frank Wyrowski and Olof Bryngdahl. 1989. Speckle-free reconstruction in digital holography. *J. Opt. Soc. Am. A* 6, 8 (Aug 1989), 1171–1174.

Xiao Xiao, Bahram Javidi, Manuel Martinez-Corral, and Adrian Stern. 2013. Advances in three-dimensional integral imaging: sensing, display, and applications [Invited]. *Applied Optics* 52, 4 (Feb 2013), 546–560.

Kazuhiro Yamaguchi, Tsubasa Ichikawa, and Yuji Sakamoto. 2011a. Calculation method for CGH considering smooth shading with polygon models. *Proc. SPIE* 7957, 795706.

Kazuhiro Yamaguchi, Tsubasa Ichikawa, and Yuji Sakamoto. 2011b. Calculation method for computer-generated holograms considering various reflectance distributions based on microfacets with various surface roughnesses. *Applied Optics* 50, 34 (Dec 2011), H195–H202.

Kazuhiro Yamaguchi and Yuji Sakamoto. 2009. Computer generated hologram with characteristics of reflection: reflectance distributions and reflected images. *Applied Optics* 48, 34 (Dec 2009), H203–H211.

Masahiro Yamaguchi. 2013. Image-based computational holography for deep 3D scene display. *Proc. SPIE* 9042, 90420A.

Masahiro Yamaguchi. 2016. Light-field and holographic three-dimensional displays [Invited]. *J. Opt. Soc. Am. A* 33, 12 (Dec 2016), 2348–2364.

Masahiro Yamaguchi, Hideaki Endoh, Toshio Honda, and Nagaaki Ohyama. 1994. High-quality recording of a full-parallax holographic stereogram with a digital diffuser. *Optics Letters* 19, 2 (Jan 1994), 135–137.

Masahiro Yamaguchi, Hideshi Hoshino, Toshio Honda, and Nagaaki Ohyama. 1993. Phase-added stereogram: calculation of hologram using computer graphics technique. *Proc. SPIE* 1914, 25–31.

Takeshi Yamaguchi, Tomohiko Fujii, and Hiroshi Yoshikawa. 2007. Computer-generated cylindrical hologram.

Takeshi Yamaguchi and Hiroshi Yoshikawa. 2011. Computer-generated image hologram. *Chinese Optics Letters* 9, 12 (2011), 20–23.

Kenji Yamamoto, Takanori Senoh, Ryutaro Oi, and Taiichiro Kurita. 2010. 8K4K-size computer generated hologram for 3-D visual system using rendering technology. In *2010 4th International Universal Communication Symposium*. 193–196.

Fahri Yaraş, Hoonjong Kang, and Levent Onural. 2009. Real-time phase-only color holographic video display system using LED illumination. *Applied Optics* 48, 34 (Dec 2009), H48–H53.

Fahri Yaraş, Hoonjong Kang, and Levent Onural. 2010. State of the Art in Holographic Displays: A Survey. *Journal of Display Technology* 6, 10 (2010), 443–454.

Toyohiko Yatagai. 1974. Three-dimensional displays using computer-generated holograms. *Optics Communications* 12, 1 (1974), 43–45.

Han-Ju Yeom and Jae-Hyeung Park. 2016. Calculation of reflectance distribution using angular spectrum convolution in mesh-based computer generated hologram. *Optics Express* 24, 17 (Aug 2016), 19801–19813.

Fucai Zhang, Ichirou Yamaguchi, and L. P. Yaroslavsky. 2004. Algorithm for reconstruction of digital holograms with adjustable magnification. *Optics Letters* 29, 14 (Jul 2004), 1668–1670.

Hao Zhang, Liangcai Cao, and Guofan Jin. 2017. Computer-generated hologram with occlusion effect using layer-based processing. *Applied Optics* 56, 13 (May 2017), F138–F143.

Hao Zhang, Liangcai Cao, Song Zong, and Guofan Jin. 2016a. Computer-generated hologram calculation using layered stereogram based inverse Fresnel diffraction, In Imaging and Applied Optics 2016. *Imaging and Applied Optics 2016*, DW5I.9.

Hao Zhang, Neil Collings, Jing Chen, Bill A. Crossland, Daping Chu, and Jinghui Xie. 2011. Full parallax three-dimensional display with occlusion effect using computer generated hologram. *Optical Engineering* 50, 7 (2011), 074003.

Hao Zhang, Yan Zhao, Liangcai Cao, and Guofan Jin. 2015. Fully computed holographic stereogram based algorithm for computer-generated holograms with accurate depth cues. *Optics Express* 23, 4 (Feb 2015), 3901–3913.

Yingxi Zhang, Juan Liu, Xin Li, and Yongtian Wang. 2016b. Fast processing method to generate gigabyte computer generated holography for three-dimensional dynamic holographic display. *Chinese Optics Letters* 14, 3 (Mar 2016), 030901.

Yaping Zhang, Jianqiang Zhang, Wei Chen, Jialing Zhang, Peng Wang, and Wei Xu. 2013. Research on three-dimensional computer-generated holographic algorithm based on conformal geometry theory. *Optics Communications* 309 (2013), 196–200.

Ya-Ping Zhang, Fan Wang, Ting-Chung Poon, Shuang Fan, and Wei Xu. 2018. Fast generation of full analytical polygon-based computer-generated holograms. *Optics Express* 26, 15 (Jul 2018), 19206–19224.

Yan Zhao, Liangcai Cao, Hao Zhang, Dezhao Kong, and Guofan Jin. 2015. Accurate calculation of computer-generated holograms using angular-spectrum layer-oriented method. *Optics Express* 23, 20 (Oct 2015), 25440–25449.

Yan Zhao, Liangcai Cao, Hao Zhang, Wei Tan, Shenghan Wu, Zheng Wang, Qiang Yang, and Guofan Jin. 2016. Time-division multiplexing holographic display using angular-spectrum layer-oriented method (Invited Paper). *Chinese Optics Letters* 14, 1 (2016), 10005–10009.

Huadong Zheng, Yingjie Yu, Tao Wang, and Linmao Dai. 2009. High-quality three-dimensional holographic display with use of multiple fractional Fourier transform. *Chinese Optics Letters* 7, 12 (Dec 2009), 1151–1154.

Long Zhu and Jian Wang. 2014. Arbitrary manipulation of spatial amplitude and phase using phase-only spatial light modulators. *Sci. Rep.* 4, 7441 (2014).

Appendices

A　NUMERICAL WAVE PROPAGATION

CGH synthesis is based on the scalar diffraction theory [Goodman 1996; Kim 2011]. Numerical propagation of a monochromatic scalar wave field is defined in accordance with the Huygens-Fresnel principle [Goodman 1996]. Given a wave field distribution $A_0(\xi, \eta)$ on the reference input plane (ξ, η) at $z = 0$, the diffraction field $A(x, y; z)$ on the output plane (x, y) at z, which is parallel to the reference plane, can be obtained using the convolution relation

$$A(x, y; z) = \iint_\Sigma A_0(\xi, \eta) h_z(x - \xi, y - \eta) d\xi d\eta, \tag{A.1}$$

where $h_z(x, y)$ represents the diffraction kernel, or the coherent point spread function (PSF) of free space propagation between the input and output planes [Kim 2011], and Σ denotes the 2D aperture defining non-zero field distribution on the input plane. The first Rayleigh-Sommerfeld (RS) solution for the Huygens-Fresnel principle describes the relation between scalar diffraction fields defined on two parallel planes, which are separated by distance $z \gg \lambda$, by the kernel

$$h_z(x, y) = \frac{z}{j\lambda} \frac{\exp\left(jk\sqrt{x^2 + y^2 + z^2}\right)}{x^2 + y^2 + z^2}, \tag{A.2}$$

where λ is the wavelength of the monochromatic light and $k = 2\pi/\lambda$ is the wavenumber. Thus, the resulting relation is given by

$$A(x, y; z) = \frac{z}{j\lambda} \iint_\Sigma \frac{A_0(\xi, \eta)}{(x - \xi)^2 + (y - \eta)^2 + z^2} \exp\left[jk\sqrt{(x - \xi)^2 + (y - \eta)^2 + z^2}\right] d\xi d\eta. \tag{A.3}$$

The so-called obliquity factor for this first RS solution is z/r, where $r = \sqrt{(x - \xi)^2 + (y - \eta)^2 + z^2}$ is the distance between the points on the input and output planes (ξ, η) and (x, y), respectively. It is essentially only this term that creates difference between various implementations of the Huygens-Fresnel principle, e.g., the two RS solutions and Fresnel-Kirchoff solution [Goodman 1996]. The angular spectrum method (ASM), which is the widely adopted implementation of RS diffraction, describes this diffraction in the spectral domain utilizing the propagating plane waves as a basis for 3D field distribution, i.e.,

$$A(x, y; z) = F^{-1}\{H_z(\vartheta_x, \vartheta_y) F\{A_0(\xi, \eta)\}|_{(\vartheta_x, \vartheta_y)}\} = F^{-1}\{H_z(\vartheta_x, \vartheta_y) G_A(\vartheta_x, \vartheta_y)\}, \tag{A.4}$$

where $F\{\cdot\}$ and $F^{-1}\{\cdot\}$ are the Fourier and inverse Fourier transform operations, $G_A(\vartheta_\xi, \vartheta_\eta)$ is the spectrum of $A_0(\xi, \eta)$ representing the coefficient of the plane wave with spatial frequencies of $(\vartheta_\xi, \vartheta_\eta)$, and $H_z(\vartheta_x, \vartheta_y)$ is the frequency response of RS diffraction given by

$$H_z(\vartheta_x, \vartheta_y) = \begin{cases} \exp\left(j2\pi z\sqrt{\frac{1}{\lambda^2} - \vartheta_x^2 - \vartheta_y^2}\right), & \text{if } \sqrt{\vartheta_x^2 + \vartheta_y^2} < \frac{1}{\lambda} \\ 0, & \text{o.w.} \end{cases} \tag{A.5}$$

The propagation direction of the plane wave with spatial frequencies $(\vartheta_\xi = \vartheta_x, \vartheta_\eta = \vartheta_y)$ is defined by the so-called wave vector $\vec{k} = (k_x, k_y, k_z)$, where $k_x = 2\pi\vartheta_x$, $k_y = 2\pi\vartheta_y$, $k_z = \sqrt{k^2 - k_x^2 - k_y^2}$, and $|\vec{k}| = 2\pi/\lambda$.

In the discrete implementation of ASM with discrete Fourier transform (DFT), the input field $A_0(\xi, \eta)$ at $z = 0$, the diffracted 3D field, and the output field $A(x, y; z)$ at z are all assumed to be periodic. The propagating plane waves are confined within the angles $\left[-\sin^{-1}\left(\frac{\lambda}{2\Delta\xi}\right), \sin^{-1}\left(\frac{\lambda}{2\Delta\xi}\right)\right]$

and $\left[-\sin^{-1}\left(\frac{\lambda}{2\Delta\eta} \right), \sin^{-1}\left(\frac{\lambda}{2\Delta\eta} \right) \right]$, which are determined by the sampling steps of the wave field, $\Delta\xi$ and $\Delta\eta$, respectively, on the input plane. In order to calculate the diffraction field accurately, the input field is usually zero padded, taking into account these angular bandwidths, and thus contributions of neighbor periods of the input field to the output field are avoided. In particular, let the finite support input field $A_0(\xi, \eta)$ exhibit $N_\xi \times N_\eta$ samples, when sampled with sampling steps of $\Delta\xi$ and $\Delta\eta$, respectively. In this case, in order to avoid aliasing in the discrete implementation of ASM, the following conditions need to be satisfied: $z \leq \frac{\sqrt{4\Delta\xi^2 - \lambda^2}}{2\lambda}(N_\xi' - N_\xi)\Delta\xi$ and $z \leq \frac{\sqrt{4\Delta\eta^2 - \lambda^2}}{2\lambda}(N_\eta' - N_\eta)\Delta\eta$, where $N_\xi' \times N_\eta'$ denotes the size of the zero-padded input field [Poon and Liu 2014].

In the paraxial approximation, fulfilled when $z^3 \gg \frac{1}{8\lambda}\left[(x - \xi)^2 + (y - \eta)^2 \right]^2$, where $(\xi, \eta) \in \Sigma$, the spherical wavefronts can be replaced with parabolic ones given by the Fresnel diffraction kernel

$$h_z(x, y) = \frac{\exp(jkz)}{j\lambda z} \exp\left[\frac{jk}{2z}(x^2 + y^2) \right], \tag{A.6}$$

which is a 2D chirp function having the following properties:

$$h_z^*(x, y) = h_{-z}(x, y), \quad h_{z_1}(x, y) * h_{z_2}(x, y) = h_{z_1 + z_2}(x, y). \tag{A.7}$$

Thus, in the paraxial regime, the propagation between two parallel planes separated by z can be computed by replacing the RS kernel in Equation (A.3) with the Fresnel kernel as

$$A(x, y; z) = \frac{\exp(jkz)}{j\lambda z} \exp\left[\frac{jk}{2z}(x^2 + y^2) \right] \iint_\Sigma A_0(\xi, \eta) \exp\left[\frac{jk}{2z}(\xi^2 + \eta^2) \right] \tag{A.8}$$
$$\exp\left[\frac{-jk}{z}(x\xi + y\eta) \right] d\xi d\eta.$$

Similar to the ASM implementation of RS diffraction, Fresnel diffraction can be also implemented in the frequency domain, using two Fourier transform operations, by replacing the frequency response of RS diffraction in Equation (A.3) with the frequency response of Fresnel diffraction given as

$$H_z(\vartheta_x, \vartheta_y) = \exp(jkz)\left[-j\pi\lambda z \left(\vartheta_x^2 + \vartheta_y^2 \right) \right]. \tag{A.9}$$

On the other hand, the Fresnel diffraction can be also implemented using a single Fourier transform operation as

$$A(x, y; z) = \frac{\exp(jkz)}{j\lambda z} \exp\left[\frac{jk}{2z}(x^2 + y^2) \right] F\left\{ A_0(\xi, \eta) \exp\left[\frac{jk}{2z}(\xi^2 + \eta^2) \right] \right\}\bigg|_{\frac{x}{\lambda z}, \frac{y}{\lambda z}}, \tag{A.10}$$

where $\left(\frac{x}{\lambda z}, \frac{y}{\lambda z} \right)$ are the spatial frequencies at which the Fourier transform is calculated. In other words, the output field at (x, y) is defined by the spectral component of the input field with spatial frequencies of $\vartheta_\xi = \frac{x}{\lambda z}$ and $\vartheta_\eta = \frac{y}{\lambda z}$.

Considering the discrete implementation of Equation (A.10) using a single DFT, one can see that the output field at z is found to be the modulated version of a periodic diffraction field obtained as the result of DFT, where the modulation function is a chirp function. The corresponding sampling steps of the output field are $\Delta x = \frac{\lambda z}{N_\xi \Delta\xi}$ and $\Delta y = \frac{\lambda z}{N_\eta \Delta\eta}$, and the central period of the periodic part is confined within $\frac{-\lambda z}{2\Delta\xi} \leq x \leq \frac{\lambda z}{2\Delta\xi}$ and $\frac{-\lambda z}{2\Delta\eta} \leq y \leq \frac{\lambda z}{2\Delta\eta}$. Thus, the sampling steps of the output field increase linearly with the propagation distance z. Given that the spectrum of $A_0(\xi, \eta)$ is confined within $[-B_\xi, B_\xi]$ and $[-B_\eta, B_\eta]$, the following conditions need to be satisfied to avoid aliasing in the discrete implementation of Equation (A.10): $B_\xi + \frac{N_\xi \Delta\xi}{2\lambda z} \leq \frac{1}{2\Delta\xi}$ and $B_\eta + \frac{N_\eta \Delta\eta}{2\lambda z} \leq \frac{1}{2\Delta\eta}$ [Poon and Liu 2014]. These conditions impose a minimum limit on the propagation distance z. The sampling step at the given propagation distance can be controlled by introducing a virtual plane and applying two

Fresnel transforms [Zhang et al. 2004]. This can be done independently of the final propagation distance and the wavelength by adjusting the distance of the virtual plane.

B NUMERICAL RECONSTRUCTION OF CGHS

Numerical reconstruction of CGHs is a necessary step in assessing the visual reconstruction quality of holograms in a controlled manner and without suffering from device limitations. Based on the observed quality, readjustments can be made on the scene and hologram parameters accordingly before printing a static hologram or setting up a holographic display. Below, such a numerical reconstruction tool is presented together with example reconstructions applied to some representative CGH techniques. The simulation tool basically models the viewing process of CGH by human eye employing a reduced eye model. It, thus, allows testing the capabilities of a given CGH method from human visual system (HVS) perspective in terms of various quality factors, such as provided perceived resolution, handling of view-dependent occlusions, delivering of correct accommodation cue, suppression of speckle noise, etc.
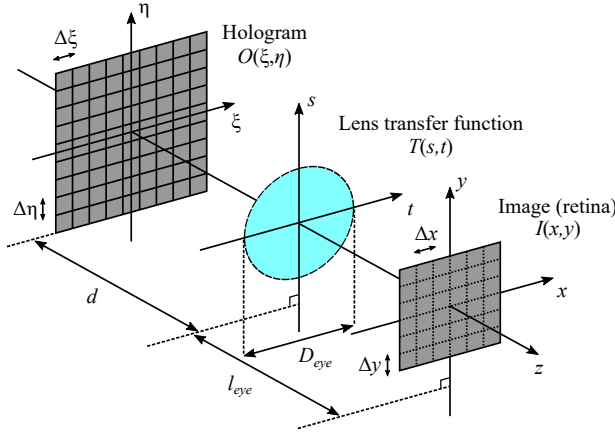

Fig. B.1. Setup for HVS based numerical CGH reconstruction simulations.

The numerical simulation of viewer perceived images is a process starting with a hologram (i.e., the complex wave field at the hologram plane) and through a process of optical field propagation operations ends up with an intensity image at the sensor plane of the simulated eye (i.e., the retina). Please note that here we refer the image encoded on the retina as the perceived image, though the perception actually involves affects of subsequent neural functions in the HVS. Let us assume the simulation setup shown in Figure B.1. A simulated human eye is placed at a distance d from the hologram plane. The eye is modeled as a conventional imaging system with thin round lens of diameter D_{eye} and focal length f_{eye} and a sensor that is placed behind the lens at distance l_{eye}. This setup results in three parallel planes to consider in the simulations and analysis: the hologram plane (ξ, η), the lens plane (s, t) and the retina plane (x, y). The sampled object field at the hologram plane (i.e., the generated hologram) is denoted by $O[m, n] = O(m\Delta\xi, n\Delta\eta)$, where $\Delta\xi$ and $\Delta\eta$ are the spatial sampling steps on the hologram plane. Denoting the discrete samples on the lens and retina planes as $[p, q]$ and $[k, l]$, respectively, and adopting the Fresnel diffraction model, the sensor plane image $I[k, l]$ is obtained as

$$I[k, l] = \left| F_{l_{eye}}\{T[p, q]F_d\{O[m, n]\}[p, q]\}[k, l] \right|^2 \qquad (B.1)$$

where $F_z\{\cdot\}$ is the discrete Fresnel propagation by distance z which is implemented using a single Fourier transformation in accordance with Equation (A.10), and $T[p, q]$ is the discrete lens transfer function given as

$$T[p, q] = \exp\left[-\frac{j\pi}{\lambda f_{eye}}\left(p\Delta s - s_{eye}\right)^2 + \left(q\Delta t - t_{eye}\right)^2\right] P(s, t). \tag{B.2}$$

In Equation (B.2), (s_{eye}, t_{eye}) denotes the lateral position of the simulated eye having the circular pupil function of

$$P(s, t) = \begin{cases} 1, & \text{if } \sqrt{\left(s - s_{eye}\right)^2 + \left(t - t_{eye}\right)^2} < \frac{D_{eye}}{2} \\ 0, & \text{o.w.} \end{cases}. \tag{B.3}$$

That is, the hologram is propagated towards the lens plane, multiplied with the lens transfer function and finally propagated to the retinal plane, from which the intensity values of the perceived image are obtained. Please note that the sampling steps on the lens plane should satisfy

$$\Delta s \leq \frac{\lambda f_{eye}}{D_{eye}}, \ \Delta t \leq \frac{\lambda f_{eye}}{D_{eye}}, \tag{B.4}$$

so that the lens transfer function is properly sampled without aliasing. The properties of the simulated eye lens can be controlled by the focal length f_{eye}, which in turn alters the transfer function. The distance l_{eye} is often kept fixed in accordance with the properties of the HVS. Thus, the focused depth of the eye can be adjusted at distance d_f by selecting the focal length as

$$f_{eye} = \left(\frac{1}{d_f} + \frac{1}{l_{eye}}\right)^{-1}. \tag{B.5}$$

The numerical simulation tool presented above is utilized to demonstrate a set of comparisons between different CGH methods. In particular, the ray-based HS and the image-order type wavefront-based method proposed in [Ichikawa et al. 2013a] are considered as two representative methods from ray-based and wavefront-based CGH categories, respectively. In the case of HS, the required perspective images of the scene are obtained by capturing pinhole views on the hologram plane, where the pinhole cameras are placed at the centers of the hogels. The hologram parameters, such as the hogel size and hologram plane sampling, are set to fulfill the requirements of the HVS, as explained in Section 4.1. For the wavefront-based CGH, the ray tracing is performed in a similar manner, casting rays from the centers of the segments on the hologram plane towards the scene. Where applicable, the hologram parameters are chosen to be equal to the HS, thus providing a fair comparison between the two methods and their properties. In addition to the simulated reconstruction images, reference images for the views are obtained by combining several pinhole images, simulating the effects of a finite size aperture [Lanman et al. 2008]. The scene for the simulations is setup as depicted in Figure B.2 including a 3D model of a car and a textured background behind it. The (fixed) hologram and simulation parameters are presented in Table B.1.
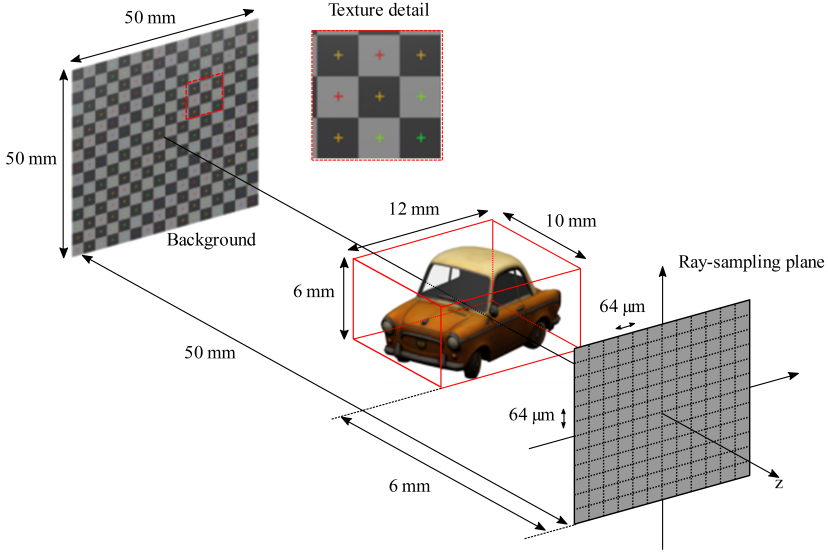
Fig. B.2. Scene setup for the simulations including a textured background and a 3D model car (Pony Cartoon by Slava Zhuravlev is licensed under CC BY 4.0).

Table B.1. Parameters of the numerical simulations.

Number of hologram samples	8192×8192
Hologram sampling ($\Delta\xi, \Delta\eta$)	2×2 μm
Segment size	64×64 μm
Wavelength	534 nm
Viewing distance d	300 mm
Pupil diameter D_{eye}	3 mm
Lens-sensor distance l_{eye}	25 mm

An important aspect of holograms is that they can deliver focus cues (accommodation and retinal defocus blur). That is, the image perceived by the viewer appears sharp, when the viewer actually accommodates (focuses) at the correct image depth, otherwise it looks blurry due to optical defocus. The accommodative response of the human eye can be evaluated by changing the focal length of the simulated lens. Comparing the reference view images on the top and bottom rows of Figure B.3(a), it is seen that different parts of the scene look blurred when the eye is focused at different depths. However, the comparison of reconstructed images from HS, column (b), and wavefront-based CGH, columns (c), clearly demonstrates the need for speckle suppression methods to do a reliable evaluation, as the speckle patterns heavily degrade the visual quality, and therefore, renders the ability to compare different methods and parameters virtually impossible. Columns (d) and (e) show the corresponding reconstruction when random averaging based speckle suppression is applied with 16 CGH frames. Please note that, although the change of focus on the model car is visible, the remaining noise still hinders the relevant information especially on the background.

The numerical reconstructions are further extended in Figure B.4 with more effective separation-based speckle suppression methods, where the speckle suppression is achieved by reconstructing
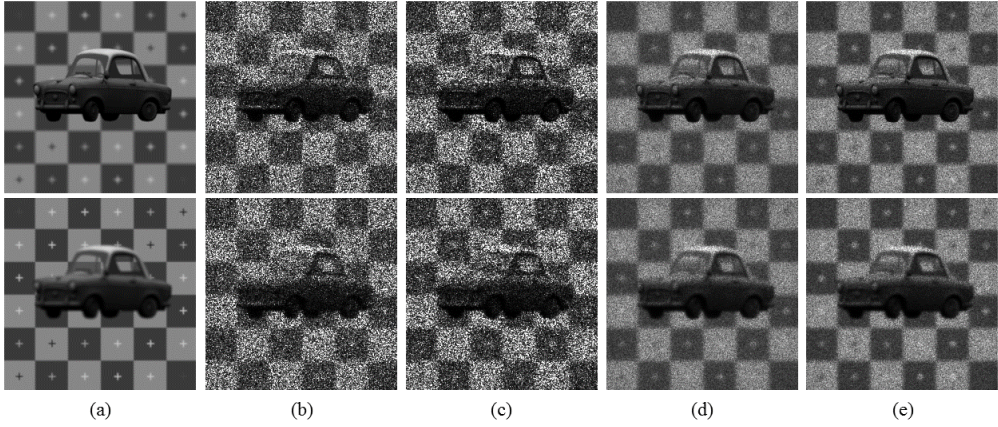
Fig. B.3. Comparison of the reference views (a), the reconstructed views from HS and wavefront-based CGH, respectively, without (b) – (c) and with (d) – (e) speckle suppression via random averaging. The simulated eye is set to focus on the model car (top row) and on the background (bottom row).
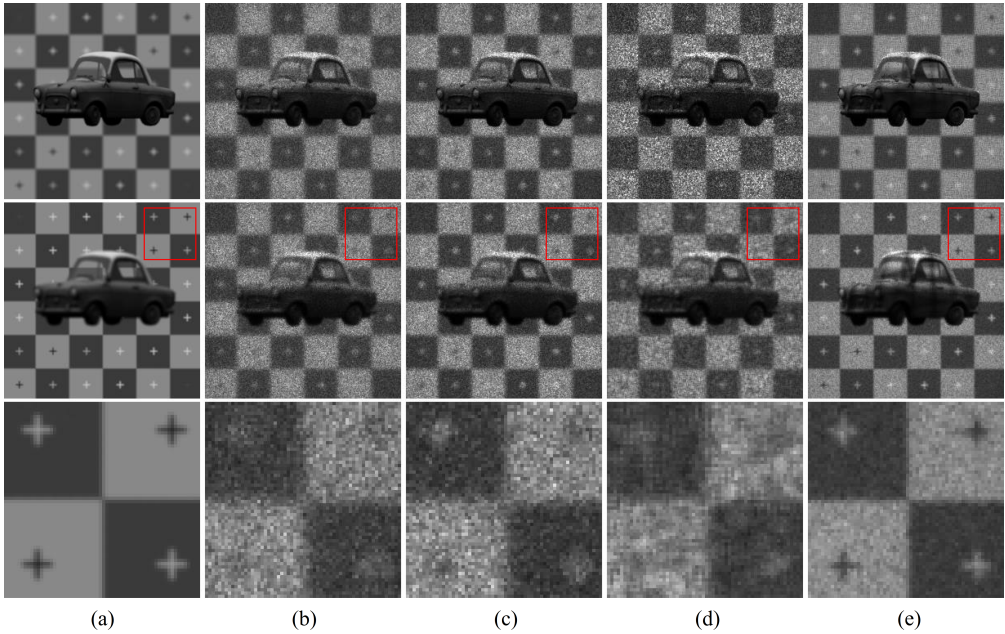

Fig. B.4. Comparison of the reference views (a), the reconstructions from HS and wavefront-based CGH, respectively, when the random averaging (b)–(c) and the separation based (d)–(e) speckle suppression is applied. The eye is focused on the model car (top row), and on the background (middle row) (zoomed-in on bottom row).

several hologram frames containing sparse sets of hogels, in the case of HS, or light rays, in the case of wavefront-based CGH [Mäkinen et al. 2018], and averaging them. The results demonstrate the limited accommodative response provided by the HS, as the background texture details cannot be

resolved appropriately, regardless of the speckle suppression method. However, for the wavefront-based CGH reconstructions, the utilized ray separation based speckle suppression method (see column (e)) results in rather sharp perceived image of the background, which supports availability of correct focus cues even for deep scenes in wavefront-based CGHs.

One can also evaluate the view-dependent properties (e.g., parallax and occlusions) by changing the position of the simulated eye. These can be observed in the reconstructions presented in Figure B.5, where the eye is moved 15 mm horizontally and vertically away from the origin. The parallax between the background and the model car can be seen, when compared to Figure B.4, with correct changes in perceived occlusions as well as the changes in the perspective of the model car. The focus cues are visible in a similar manner to the center views, as highlighted in the magnified detail images. The intensity variations that are visible in stripes on the surface of the car are inherent to ray-separation based speckle suppression method [Mäkinen et al. 2018].

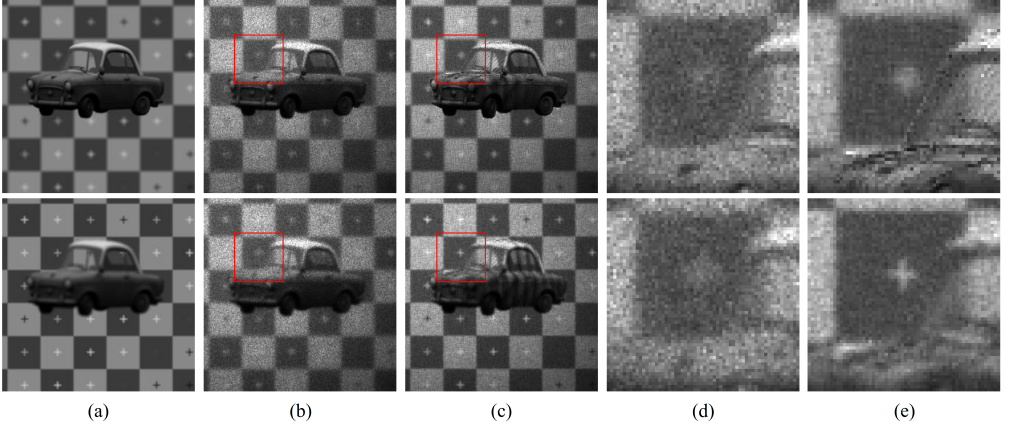|				
(a)	(b)	(c)	(d)	(e)

Fig. B.5. Comparison of the reference views (a), the reconstructions from HS when the random averaging based speckle suppression is applied (b), zoomed-in on (d), and the reconstructions from wavefront-based CGH when the ray separation based speckle suppression is applied (c), zoomed-in on (e). The eye is at (s_{eye}, t_{eye}) = (15 mm,15 mm) and it is focused on the model car (top row) and on the background (bottom row).